

# The extremely young planetary nebula M 3-27: an analysis of its evolution, physical conditions and abundances

Francisco Ruiz-Escobedo<sup>1</sup>\* Miriam Peña,<sup>1</sup> and Ana Valeria Beltrán-Sánchez<sup>1,2</sup>

<sup>1</sup>*Instituto de Astronomía, Universidad Nacional Autónoma de México, Apdo. Postal 70264, Ciudad de México, México*

<sup>2</sup>*Facultad de Ciencias, Universidad Nacional Autónoma de México, Ciudad de México, México*

Accepted XXX. Received YYY; in original form ZZZ

## ABSTRACT

Spectrophotometric data of the young planetary nebula M 3-27, from 2004 to 2021, are presented and discussed. We corroborate that the H I Balmer lines present features indicating they are emitted by the central star, therefore He I lines were used to correct line fluxes by effects of reddening. Important variability on the nebular emission lines between 1964 to 2021, probably related to density changes in the nebula, is reported. Diagnostic diagrams to derive electron temperatures and densities have been constructed. The nebula shows a very large density contrast with an inner density of the order of  $10^7 \text{ cm}^{-3}$  and an outer density of about  $10^3 - 10^4 \text{ cm}^{-3}$ . With these values of density, electron temperatures of 16,000 – 18,000 K have been found from collisionally excited lines. Due to the central star emits in the H<sup>+</sup> lines, ionic abundances relative to He<sup>+</sup> were calculated from collisionally excited and recombination lines, and scaled to H<sup>+</sup> by considering that He<sup>+</sup>/H<sup>+</sup> = He/H = 0.11. ADF(O<sup>+2</sup>) values were also determined. Total abundance values obtained indicate sub-solar abundances, similarly to what is found in other comparable objects like IC 4997.

**Key words:** planetary nebulae: individual: M 3-27 – ISM: abundances – ISM: kinematics and dynamics

## 1 INTRODUCTION

Planetary nebulae (PNe) are formed by the ejection of parts of the stellar atmosphere during advanced stages of evolution of low-intermediate mass stars. The ejecta, initially neutral or molecular, expands at velocities of about 10–20 km s<sup>-1</sup> and later it is photoionized by the energetic photons of the star when it evolves from the Asymptotic Giant Branch (AGB) phase towards higher effective temperatures and reaches temperatures larger than 25,000 K. The stellar transition between the post-AGB and the PN phase is not well known, it is not smooth and substantial photometric and spectral changes might occur in few years.

There are few stars known to be in this transition period, presenting very young planetary nebulae. Some of them are IC 4997, the Stingray nebula, VV 8, PM 1-322, and a few others.

In this work, we analyse spectrophotometric data of the very young and compact PN M 3-27 whose interesting behaviour has been studied since 50 years ago (Kohoutek 1968; Adams 1975; Ahern 1978; Barker 1978; Feibelman 1985; Miranda et al. 1997; Wesson et al. 2005). The main characteristics of M 3-27 are listed in Table 1. Previous works showed the presence of two density zones inside the nebula, an inner zone of  $n_e \geq 10^6 \text{ cm}^{-3}$  and a compact outer zone of  $n_e \sim 10^3 - 10^4 \text{ cm}^{-3}$ .

Given the high density of the nebula, it has been difficult to determine a proper value of  $T_e$  using plasma line diagnostics. Ahern (1978) estimated a value of  $T_e = 16,400 \text{ K}$  by comparing the line

ratios of [O III]λ5007 and [Ne III]λ3869 according to the methodology presented by Ahern (1975). Wesson et al. (2005) determined a  $T_e = 13,000 \text{ K}$  using the line ratio [O III] λλ4959/4363 by assuming a density  $n_e = 10^7 \text{ cm}^{-3}$ , estimated from high-order H I Balmer lines.

By means of position-velocity diagrams (PVD), Miranda et al. (1997) studied the line profiles and kinematics of this object. They found that the Hα line has a kinematic profile different than those of [S II] and [N II] lines. Hα shows a double peak, much more intense in the red than in the blue, and wide wings extending up to ±1500 km s<sup>-1</sup>, possible due to Rayleigh-Raman dispersion<sup>1</sup> occurring in a very dense zone near the central star. In addition, faint Hα emission can be traced up to about ±12 arcsec from the stellar position, which is not shown by the heavy element lines. These latter lines and radio continuum emission at 3.6 cm are originated in a compact inner shell not spatially resolved (FWHM ≤ 1.4 arcsec). Miranda et al. (1997) estimated a kinematic age lower than 580 yr for the inner shell of this young PN.

We have studied this object as part of a project devoted to analyse young and dense PNe, whose first results were published by Ruiz-

<sup>1</sup> Rayleigh and Raman scattering are processes of photon scattering by atoms or molecules. Lee & Hyung (2000) and Arrieta & Torres-Peimbert (2003) suggested that the main mechanism of formation of very broad wings on Hα lines in young planetary nebulae is the Raman scattering of near-Lyβ photons produced by a dense atomic H I region near to the central star. However, photons may suffer a series of Raman and Rayleigh scattering (in which an incident Hα photon is scattered as another Hα photon) before leaving this dense neutral region.

\* E-mail: fdruiz@astro.unam.mx

**Table 1.** Characteristics of M 3-27

Names	Gal. coord. (deg)	RA (2000) (hr:min:s)	Dec (2000) (deg:min:sec)	Size	Parallax (mas) Gaia DR3	$v_{rad}$ (LSR) (km s <sup>-1</sup> )	Comments
PN G043.6+11.6 IRAS 18255*14.27	43.3554 +11.698	18:27:48	+14:29:06	Stellar	0.1468 <sup>a</sup>	-24 <sup>b</sup>	Wide H $\alpha$ Double peak H I lines

<sup>a</sup> Gaia Collaboration et al. (2016, 2023) <sup>b</sup> Miranda et al. (1997)

Escobedo & Peña (2022). The general purpose of the project is to determine physical conditions and chemical composition of these young nebulae, with special emphasis in determining the Abundance Discrepancy Factors (ADF) between measurements from collisionally excited lines (CELs) and recombination lines ORLs<sup>2</sup>.

This paper is organized as follows: In §1 we present the introduction with the general characteristics of M 3-27. In §2, observations and data reduction are described. In §3 we analyse the calibrated line intensities to determine reddening corrections based He I lines and analyse the temporal variations of line intensities. In §4 the line profiles are analysed. In §5 physical conditions and chemical abundances from collisionally excited lines and from recombination lines are determined and discussed. Line profiles and kinematics of the plasma are discussed in §6. In §7 we present the discussion of our results and our conclusions can be found in §8.

## 2 OBSERVATIONS

Spectrophotometric data of M 3-27 were obtained at the Observatorio Astronómico Nacional San Pedro Mártir (OAN-SPM) at Baja California, México, between the years 2004 to 2022. Two spectrographs of different resolution, attached to the 2.1-m telescope, were used: the Boller & Chivens (B&Ch) spectrograph of low-medium dispersion (resolution  $R(\lambda/\delta\lambda)$  of 685 at 5000 Å) and the REOSC-Echelle spectrograph of high dispersion (resolution  $R \sim 16,000$ – $18,000$  at 5000 Å). The log of observations is presented in Table 2.

### 2.1 Data reduction

IRAF<sup>3</sup> tasks were used for data reduction. The 2D B&Ch frames were bias subtracted and flat fielded. Spectra were extracted (extraction window width included all the observed flux) and wavelength and flux calibrated. A Cu-Ar lamp, observed after each exposure, was used for wavelength calibration of B&Ch observations. The standard stars Feige 34, Feige 66 and BD+30 2642 were observed each night for flux calibration with a slit width of 500  $\mu$ m (6.6 arcsec), in order to include all the stellar flux.

2D REOSC-Echelle spectra were bias subtracted but no flat fielding was applied. Spectra were extracted from all the available orders, the extraction window included all the flux. Wavelength calibration was applied with a Th-Ar lamp obtained after each scientific observation. Standard stars from the list by Hamuy et al. (1992) were observed for flux calibration.

All observations were also corrected by effects of atmospheric

extinction, using the curve determined by Schuster & Parrao (2001) for the OAN-SPM sky.

Calibrated spectra of different epochs have been used to determine variations of the emission lines, to analyse the line profiles, to determine the reddening, the physical conditions and the nebular ionic and total abundances. Fluxes from available lines in each spectrum were measured using IRAF's *splot* task and normalized to the flux of H $\beta$  ( $H\beta = 100$ ). Errors in line fluxes were estimated following Tresse et al. (1999) procedure. For REOSC-Echelle spectra, FWHM (full width at half-maximum) were also measured and corrected by effects of instrumental and thermal broadening (assuming the electron temperature derived in each observation), subtracted in quadrature from the measured FWHM. For physical conditions and abundances, errors were estimated using Monte Carlo simulations, a set of 400 random points was generated following a normal distribution centred on each observed line intensity.

## 3 REDDENING CORRECTION

In very high-density ionized gas, when the nebula is optically thick to H Lyman series and partially thick to H Balmer series, particularly thick to H $\beta$ , the photons will be self-absorbed and will reappear in a cascade as P $\alpha$ , H $\alpha$  and Ly $\alpha$  photons. Thus the H $\alpha$  photons emitted will increase and H $\beta$  photons will decrease, increasing the observed H $\alpha$ /H $\beta$  intensity ratio. Then such a ratio is not useful to determine the reddening. Capriotti (1964) calculated the theoretical values of the Balmer series in case of self-absorption for different optical depths. We have used Capriotti's procedure to determine  $c(H\beta)$  for the different observations presented in the literature (Kohoutek 1968; Adams 1975; Ahern 1978; Barker 1978, and ours in this paper) finding that the  $c(H\beta)$  value seems to vary with time, increasing from 0.50–0.75 for the observations of the seventies to values larger than 1.35–1.95 in the years from 2004 to 2021, due to the changes in H $\alpha$ /H $\beta$  value probably produced by changes in the emission of the central star.

Due to the above, we consider that such a procedure is not appropriate to determine the external reddening for the OAN-SPM observations. Instead we decided to determine it by using the He I lines following the procedure recently proposed by Zamora et al. (2022). Such a procedure consists in using the intensities of the optical He I singlet lines  $\lambda\lambda 4922, 6678, 7281$  and the triplet  $\lambda 5876$  line, relative to  $\lambda 6678$ , because their theoretical intensities are unaffected by optical depth and density effects, even for densities as large as  $10^8$  cm<sup>-3</sup>, contrary to what occurs with other He I triplet lines (Rodríguez 2020; Zamora et al. 2022).

The expression used to calculate  $c(H\beta)$  is:

$$\log(F_\lambda/F_{ref}) - \log(I_\lambda/I_{ref}) = -c(H\beta)(f(\lambda) - f(\lambda_{ref})). \quad (1)$$

where  $F_\lambda$  are the observed fluxes,  $I_\lambda$  are the de-reddened fluxes, and  $f(\lambda)$  is the extinction law given by Cardelli et al. (1989), assuming a ratio of total to selective extinction  $R_V = 3.1$ . The reference wavelength ( $\lambda_{ref}$ ) is  $\lambda 6678$  Å, which corresponds to the most intense of

<sup>2</sup> The ADF is defined as the ratio of the abundance derived from ORLs to the abundance derived from CELs:  $ADF(X^{+i}) = X_{ORLs}^{+i} / X_{CELs}^{+i}$ .

<sup>3</sup> IRAF is distributed by the National Optical Observatory, which is operated by the Associated Universities for Research in Astronomy, Inc., under contract to the National Science Foundation.

**Table 2.** Log of observations for M 3-27

Obs. date	Spectrograph <sup>(a)</sup>	#exp × $t_{exp}$ (s)	Slit size	spectral resolution		$\lambda$ range Å	Binning pix×pix Å×''	Airmass (average)
				Å/pix	R(5000Å)			
22/04/2004	B&Ch (300 l mm <sup>-1</sup> ) <sup>(b)</sup>	2 × 60	5'×4"	2.23	567	3450–7400	2×2 7.0×0.35	1.04
25/04/2004	REOSC-Echelle	2 × 900	13.3''×4"	0.34	16,000	3600–6800	2×2 0.3×0.35	1.13
30/06/2019	REOSC-Echelle	3 × 1800	13.3''×2"	0.30	18,000	3600–7200	1×1 0.2×0.18	1.05
04/05/2021	B&Ch (600 l mm <sup>-1</sup> )	3 × 900	5'×4"	1.54	685	3800–5950	2×2 5.4×0.35	1.07
05/05/2021	B&Ch (600 l mm <sup>-1</sup> )	2 × 900	5'×4"	1.54	685	5200–7300	2×2 5.4×0.35	1.07
06/05/2021	B&Ch (300 l mm <sup>-1</sup> )	2 × 300	5'×4"	2.23	567	3450–7400	2×2 7.0×0.35	1.24
02/10/2021	REOSC-Echelle	3 × 1800	13.3''×4"	0.34	16,000	3600–7200	2×2 0.3×0.35	1.25
16/08/2022	REOSC-Echelle	3 × 1800	13.3''×2"	0.30	18,000	3600–7200	1×1 0.2×0.18	1.28

(a) The P.A. of the slit for B&Ch observations was always E-W, for all REOSC-Echelle it was E-W, except for 2021 when it was N-S.

(b) In parenthesis, the grating used.

the He I singlet lines. This line will be used to normalize the line intensities.

By using PYNEB Luridiana et al. (2015), the theoretical intensities  $I_\lambda$  were calculated for a density of  $10^7 \text{ cm}^{-3}$  and a temperature of  $10^4 \text{ K}$ , the atomic parameters used are those by Porter et al. (2012, 2013).

The ratios of He I observed fluxes and dereddened fluxes for all the observations from 2004 to 2021, normalized to the line  $\lambda 6678 \text{ \AA}$  as said above, and their values of  $f(\lambda)$  were plotted in the plane  $\log(F_\lambda/F_{ref}) - \log(I_\lambda/I_{ref})$  vs.  $f(\lambda) - f(\lambda_{ref})$  (see Fig. 1). A linear regression was applied to all the plots, deriving in each case the  $c(H\beta)$  value which is the slope of the calculated lines.

The results are presented in Table 3 where the RMS of the regression is adopted as the error for the determined  $c(H\beta)$ . The value  $R^2$  of the regression is given. For each observation, the  $c(H\beta)$  values derived this way were used to deredden the spectra.

The observed and dereddened fluxes relative to  $H\beta$  and the FWHM of all the detected lines, for all the observations, are presented in a table on-line. In Table 4 we present an example of such a table.

### 3.1 Temporal variations of line intensities

Fig. 2 shows the temporal evolution of some important lines in the period from 1964 to 2021. The data from 1964 to 1978 were obtained from Kohoutek (1968); Adams (1975); Ahern (1978) Barker (1978). In Fig. 2 (up, left) the evolution of lines [O III] $\lambda 5007$ ,  $\lambda 4363$  and [Ne III] $\lambda 3869$  relative to  $H\beta$  are presented. It is observed that the nebular line [O III] $\lambda 5007$  diminished by a factor of 2.7 in this period, while the auroral line [O III] $\lambda 4363$  and the [Ne III] $\lambda 3869$  line do not show significant variations. This is a consequence of the critical density ( $n_{crit}$ ) that is lower for  $\lambda 5007$  than for the other lines (see Table 5). In the case of H I Balmer lines (Fig. 2 (up, right)) impressive changes are found, the  $H\alpha/H\beta$  ratio increased by a factor of 4 in the period of 50 years, from  $\sim 4$  during 1970 to  $\sim 12$  in 2021, while  $H\gamma$  and  $H\delta$  show no significant variations relative to  $H\beta$ . This confirms that  $H\alpha$  is partially emitted by the central star and its variations can be attributed to changes in the stellar emission.

The behaviour of other heavy element lines is shown in Fig. 2 (low, left) where the most large variation is presented by [O II] $\lambda 3727+$  nebular lines (the addition of [O II] $\lambda 3726$  and  $\lambda 3729$  lines) which decreased by a factor of 4 in the period from 1970 to 2020, from  $\sim 0.4H\beta$  in 1970 to  $< 0.1H\beta$  in 2020, while the [O II]  $\lambda 7325+$  auroral lines (the addition of [O II] $\lambda 7319$ ,  $\lambda 7320$ ,  $\lambda 7329$ , and  $\lambda 7330$  lines) show small variations. Other lines present smaller changes. He I  $\lambda 5876$  increased by a factor of 1.4 in 2004 while [S II]  $\lambda 6717$

did not vary significantly. In Fig. 2 (low, right) the behaviour of [N II]  $\lambda 6584$  nebular line and  $\lambda 5755$  auroral line are shown, in this case the nebular line  $\lambda 6584$  had varied significantly while the auroral line  $\lambda 5755$  presents small changes.

All the above is an effect of the critical densities that are lower for the lines [O II] $\lambda 3727+$  and [N II] $\lambda 6584$  than for the others. The critical densities derived from PYNEB for the lines mentioned here are tabulated in Table 5. The atomic parameters used are listed in Table C1, and the temperature assumed was 17,000 K which is an average value of the temperatures derived for the different observations (see Table 6).

As H I lines show characteristics indicating they are emitted by the stellar atmosphere and present variations through time, we also analysed the evolution of line intensities relative to He I  $\lambda 5876$  line, which is emitted by the nebula. In Figure 3, we present the temporal evolution of the intensities of the same lines analysed above but normalized to the mentioned He I line. For the observations from the 1970s, the He I  $\lambda 5876$  line is only reported in the data from Ahern (1978) and Barker (1978), however the line intensities show the same behaviour as it was found for the normalization to  $H\beta$ , highlighting the suppression of the emission of nebular lines of [O II], [N II] and [O III].

## 4 THE LINES PROFILES

In Fig. 4 the line profiles of  $H\alpha$ ,  $H\beta$ , [O III] $\lambda 4959$  and He I  $\lambda 5876$  are shown from the 2019 high resolution REOSC-Echelle observations. It is found that both H I lines show double peak with a faint component appearing to the blue. The red component is very intense in comparison with the blue one. Both peaks are separated by about  $70 \text{ km s}^{-1}$ . Such a profile was already found by Miranda et al. (1997) who reported that  $H\alpha$  exhibits a type III P-Cygni profile with two emissions at  $v_{LSR} -84$  and  $-7 \text{ km s}^{-1}$ , separated by an absorption at  $-55 \text{ km s}^{-1}$ . In addition  $H\alpha$  shows very extended wings traced up to  $\pm 1500 \text{ km s}^{-1}$ . We have found this profile in all the Balmer lines at least up to  $H\delta$ . The H I line profiles are different from the profiles of He I and heavy element lines which show a unique peak at a systemic velocity  $v_{hel}$  of  $\sim -70 \text{ km s}^{-1}$  as shown in Fig. 4. Such peak coincides better with the position of the absorption shown by the Balmer lines, which indicates that the Balmer lines originate mainly in a different zone than the He I and the heavy element lines, most probably in the atmosphere of the central star. This will complicate the calculus of abundances as it will be seen in the next sections.

An interesting fact found in this work is that the line profile of  $H\alpha$  seems to have changed with time (see Fig. 5). In particular, the blue

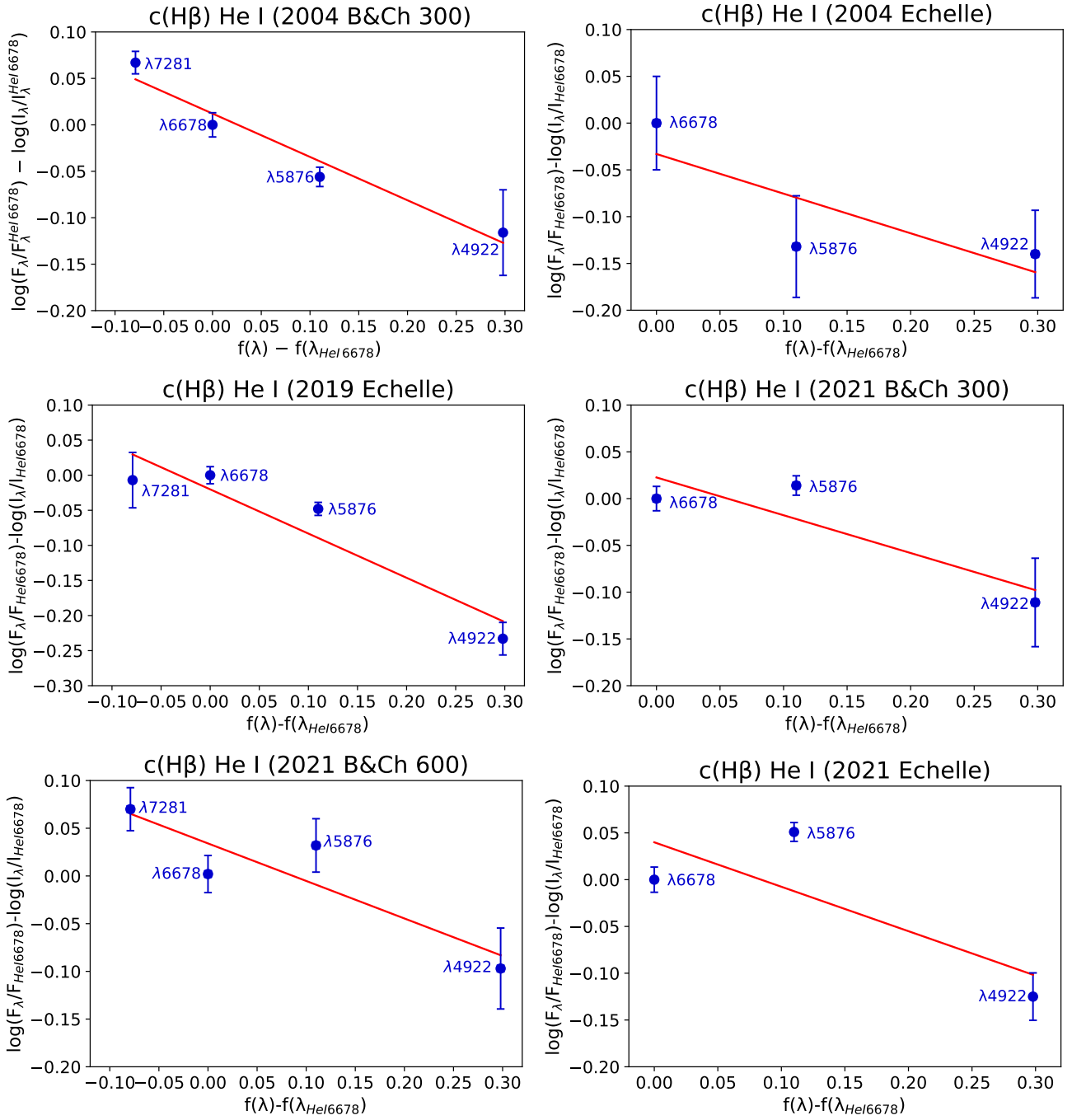


**Figure 1.** Extinction determination using the He I lines.  $c(H\beta)$  is the slope of the calculated lines.

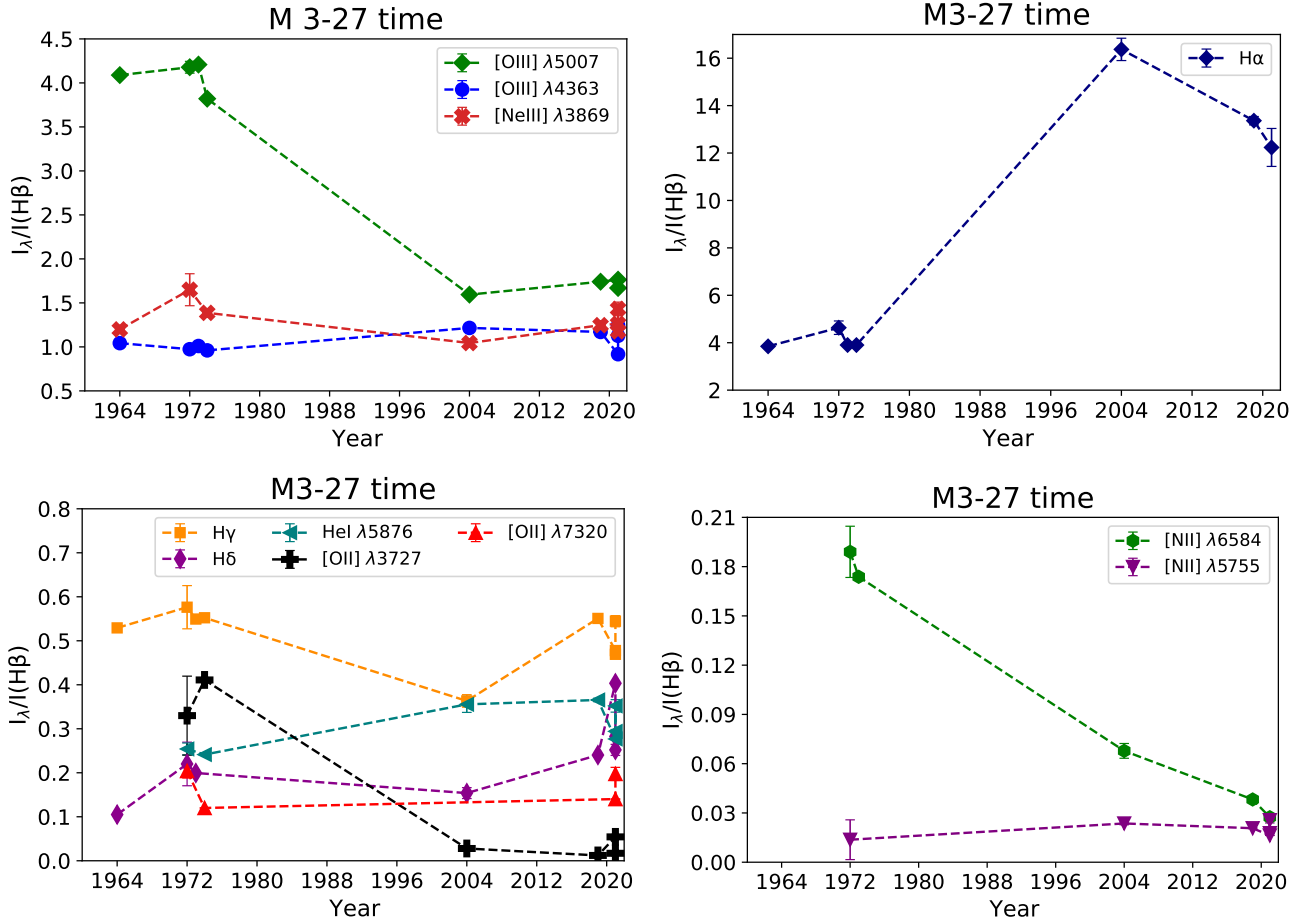
**Table 3.** Logarithmic reddening  $c(H\beta)$  from He I lines for M3-27

Year	Obs	$c(H\beta)$	RMS	$R^2$	He I observed lines
2004	B&Ch (300 l/mm)	0.47	0.02	0.95	4922, 5876, 6678, 7281
2004	REOSC-Echelle	0.42	0.04	0.66	4922, 5876, 6678
2019	REOSC-Echelle	0.63	0.03	0.89	4922, 5876, 6678, 7281
2021	B&Ch (300 l/mm)	0.40	0.03	0.79	4922, 5876, 6678
2021	B&Ch (600 l/mm)	0.46	0.04	0.72	4922, 5876, 6678, 7281
2021	REOSC-Echelle	0.48	0.05	0.63	4922, 5876, 6678

**Table 4.** Example: observed ( $F_\lambda$ ) and dereddened ( $I_\lambda$ ) fluxes normalized to  $H\beta = 100$ , their absolute errors, FWHM of line widths and expansion and heliocentric velocities<sup>a</sup>.

Ion	$\lambda_0$ (Å)	$\lambda_{obs}$ (Å)	$F_\lambda/F(H\beta)$	$\delta(F_\lambda)$	$I_\lambda/I(H\beta)$	$\delta(I_\lambda)$	FWHM (Å)	$v_{exp}$ (km s <sup>-1</sup> )	$v_{rad}$ (km s <sup>-1</sup> )
H25	3669.47	3668.66	0.28	0.11	0.46	0.19	0.23	9.59	-66.35
H24	3671.48	3670.67	0.51	0.17	0.83	0.27	0.26	10.79	-66.31
H23	3673.76	3672.90	0.61	0.27	0.97	0.43	0.52	21.31	-70.27
H22	3676.37	3675.50	0.73	0.21	1.17	0.34	0.71	28.99	-70.71
H21	3679.36	3678.50	0.96	0.22	1.53	0.36	0.22	9.15	-70.41
H20	3682.81	3681.92	1.13	0.27	1.80	0.43	0.41	16.87	-72.13
H19	3686.83	3686.03	1.31	0.39	2.10	0.62	0.33	13.38	-65.22
H18	3691.56	3690.68	1.06	0.36	1.68	0.58	0.25	10.25	-71.39
H17	3697.15	3696.39	1.81	0.51	2.88	0.81	0.49	20.08	-61.39
H16	3703.86	3703.03	2.12	0.48	3.40	0.77	0.59	23.79	-66.94
He I	3705.04	3704.10	0.92	0.35	1.47	0.57	0.52	20.88	-75.75
H15	3711.97	3711.14	2.21	0.31	3.54	0.50	0.76	30.71	-66.72
H14+[S III]	3721.83	3720.94	4.01	0.34	6.41	0.56	0.69	27.79	-72.10
[O II]	3726.03	3725.28	0.48	0.11	0.76	0.18	0.36	14.51	-60.75
[O II]	3728.82	3728.08	0.29	0.11	0.46	0.17	0.84	33.88	-59.58
H13	3734.37	3733.52	3.12	0.26	4.95	0.43	0.73	29.21	-67.92
H12	3750.15	3749.34	3.84	0.55	6.07	0.88	0.80	31.95	-64.84
H11	3770.63	3769.81	4.37	0.30	6.80	0.49	0.42	16.52	-64.96

<sup>a</sup>  $F_\lambda$ : observed flux,  $\delta(F_\lambda)$ : error,  $I_\lambda$ : dereddened flux,  $\delta(I_\lambda)$ : error,  $v_{exp}$ : expansion velocity,  $v_{rad}$ : heliocentric velocity. The complete table, including all the observations, is on-line-material.


**Figure 2.** Temporal evolution of the dereddened intensities of important lines. In these plots, lines are normalized to  $H\beta = 1$ .

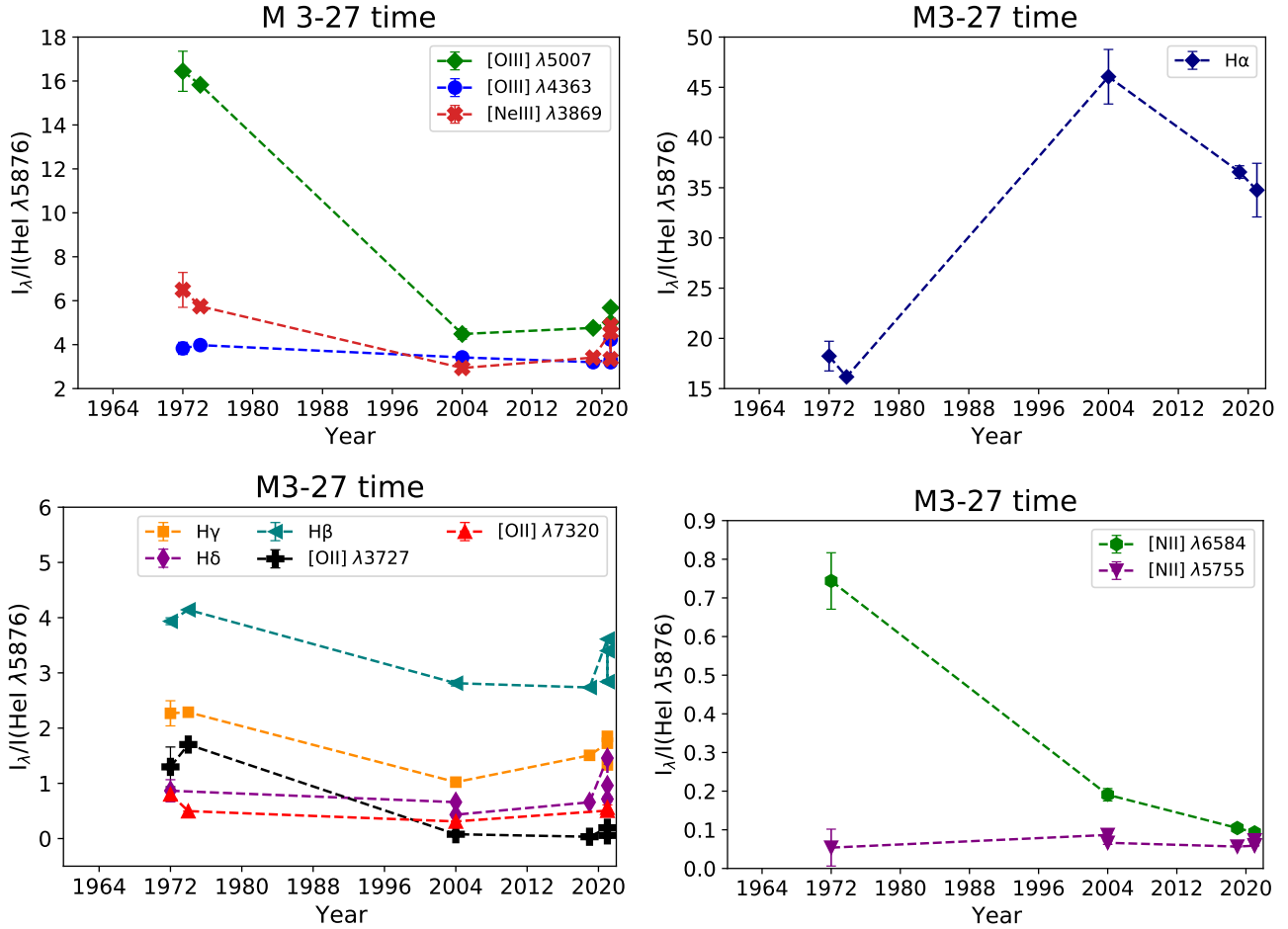


**Figure 3.** Temporal evolution of the dereddened intensities of important lines relatives to He I line  $\lambda 5876$ .

**Table 5.** Critical electron densities ( $n_{crit}$ ) for lines of interest at  $T_e = 1.7 \times 10^4$  K.

Ion	$\lambda$ (Å)	$n_{crit}^a$ ( $\text{cm}^{-3}$ )
[O II]	3726	$4.97 \times 10^3$
[O II]	3729	$1.43 \times 10^3$
[O II]	7325	$4.92 \times 10^6$
[O III]	4363	$3.06 \times 10^7$
[O III]	5007	$8.15 \times 10^5$
[N II]	5755	$1.95 \times 10^7$
[N II]	6584	$1.09 \times 10^5$
[Ne III]	3869	$1.33 \times 10^7$
[S II]	6717	$1.44 \times 10^3$
[S II]	6731	$3.89 \times 10^3$
[S II]	4068	$2.22 \times 10^6$
[Ar III]	5191	$5.06 \times 10^7$
[Ar III]	7136	$6.92 \times 10^6$
[Ar IV]	4711	$1.96 \times 10^4$
[Ar IV]	4740	$1.20 \times 10^5$
[Ar IV]	7170	$2.16 \times 10^7$
[Cl III]	5518	$7.34 \times 10^3$
[Cl III]	5538	$4.01 \times 10^4$

<sup>a</sup> Critical densities calculated with PyNEB using atomic data presented in Appendix C.

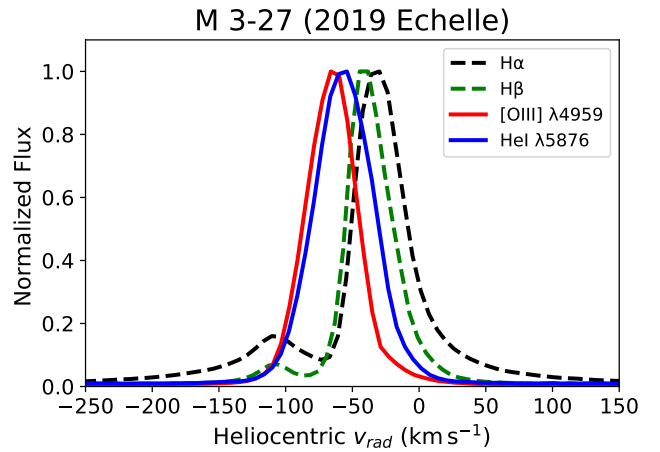


**Figure 4.** Profiles and heliocentric radial velocities of important lines.

component of the profile was more intense in 2004 than it was in the period 2019 to 2022. The observations reported by [Miranda et al. \(1997\)](#), obtained in 1993, also shows a blue component similar to the ones of the 2019–2022 period, with an intensity of about 0.2 the value for the red component. However [Tamura et al. \(1990\)](#) shows a

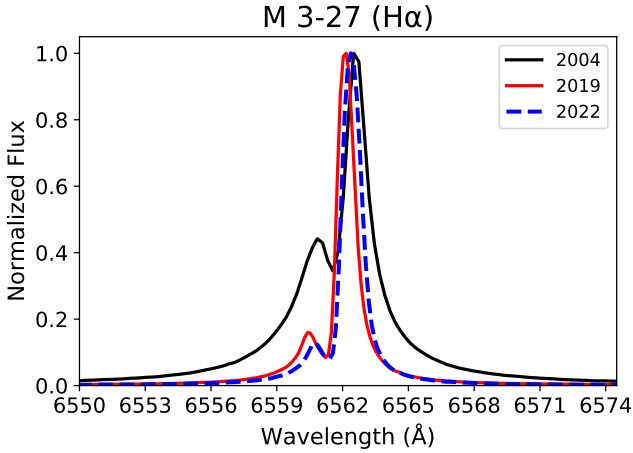


**Figure 5.** Variations of the stellar profile of H $\alpha$  with time. Notice that the blue component was more intense in 2004. H $\alpha$  profile from 2021 spectrum is not presented due it is saturated.

single profile for H $\alpha$  from observations obtained by K. M. Shibata previous to 1988.

## 5 PHYSICAL CONDITIONS AND CHEMICAL ABUNDANCES

Physical conditions,  $T_e$  and  $n_e$ , were calculated using PyNEB (Luridiana et al. 2015). This was done by adopting the line intensities relative to H $\beta$  presented in Table 4, determined including all the observed emission (in the case of H I Balmer lines both components were included), corrected by reddening and using the atomic data presented in Table C1. Several plasma diagnostic intensity ratios from the collisionally excited lines (CELs) of different ions are available to determine electron temperature and densities. The behaviour of these diagnostic lines can be observed in the diagnostic diagrams (Figure 6), which were constructed using PyNEB for OAN-SPM observations between 2004 and 2021.

The diagnostic diagrams show that the “traditional” auroral-nebular line intensity ratios normally used to determine electron temperature, such as [O III]  $\lambda\lambda(5007+4959)/4363$ , [N II]  $\lambda\lambda(6584+6548)/5755$  and [Ar III]  $\lambda\lambda 7136/5192$ , cannot be used with such a purpose in M 3-27 due to such ratios are more indicative of the electron density. A density of the order of  $n_e \sim 10^7 \text{ cm}^{-3}$ , higher than the critical density of some nebular lines, are derived from these ratios. On the other hand, the [S II]  $\lambda\lambda 6731/6716$  and [O II]  $\lambda\lambda 3729/3726$  intensity ratios indicate a much lower density ( $n_e \sim 10^3 \text{ cm}^{-3}$ ). It is clear from such diagrams that M 3-27 has a large density contrast, being much denser in the inner zone.

The contribution of recombination to the intensity of the nebular line [N II]  $\lambda 5755$  was determined using the relation proposed by Liu et al. (2000), which requires the calculation of the recombination abundance of N $^{+2}$  (see Tab. 8). This contribution was calculated to be < 7% for the REOSC-Echelle observations.

Thus, the determination of an electronic temperature from the CELs of M 3-27 by using the “traditional” method, based on the intersection of a density sensitive line diagnostic with a temperature sensitive line diagnostic, is not possible. To estimate the  $T_e$ , we decided to use a methodology similar to the one presented by Wesson et al. (2005) for the analysis of this same object: by assum-

ing a density  $n_e = 10^7 \text{ cm}^{-3}$ , (as estimated from our diagnostic diagrams, as explained above),  $T_e$  is determined from the [O III]  $\lambda\lambda(5007+4959)/4363$  line ratio. Although it is possible to determine a  $T_e$  from [O I]  $\lambda\lambda(6364+6300)/5577$  line ratio, this  $T_e$  value was not used because it corresponds to an outer and neutral zone of the nebula where the gas is not ionized. In Fig. 6  $n_e = 10^7 \text{ cm}^{-3}$  is plotted as a vertical solid black line and by using PyNEB *getTemden* routine the value for  $T_e$  was computed. This was applied to each OAN-SPM observations and the respective  $T_e$  was assumed for the whole nebula, for each observation.

Physical conditions from optical recombination lines (ORLs) were also determined for some of the observations. The temperature from H I Balmer Jump (BJ) was only determined for the REOSC-Echelle 2019 data, following the procedure given by Liu et al. (2001). However, the derived value is very uncertain and was not used for further calculations.

The temperature from He I was determined from the line ratio  $\lambda\lambda 7281/6678$  using the relation given by Zhang et al. (2005), which is based on the Benjamin et al. (1999) atomic parameters<sup>4</sup>.  $T_e(\text{He I})$  could only be determined for Boller & Chivens observations from 2004 (300 l mm $^{-1}$ ) and 2021 (600 l mm $^{-1}$ ) and REOSC-Echelle 2019, while for the other observations, the  $\lambda 7281$  line was outside the wavelength range of the spectra.

The  $T_e(\text{He I})$  was adopted for the recombination lines of heavy elements. O II density was determined from the  $\lambda\lambda 4649/4661$  line ratio only for REOSC-Echelle 2019 spectrum.

In Table 6, the values of temperature and density from CELs and ORLs are listed for the different epochs of observation. The more complete data correspond to the REOSC-Echelle 2019 observations, where electron temperatures from CELs have values from 11,100 K for [O I] to 16,800 K for [O III] and electron densities go from a few thousand  $\text{cm}^{-3}$  for the outer zone to several times  $10^7 \text{ cm}^{-3}$  in the inner zone. As expected, He I temperatures, with values between  $\sim 8300 - 10,500$  K, are lower than the temperatures derived from CELs. The values listed in this table will be used to determine ionic abundances.

### 5.1 Ionic and total abundances

Given that the H I Balmer lines seem to be emitted partially by the star, it is inadequate to calculate the chemical abundances following the usual procedure, with the emission line intensities relative to H $\beta$ . However, considering that previous authors have calculated the chemistry in M 3-27 by following the usual procedure we decided to calculate ionic and total abundances relative to H $^{+}$  and the results are shown in Appendix A. These calculations were performed using the routine *getIonAbundance* from PyNEB. It is clear that these results are not confident due to the contamination by the central star but we include them here for comparison and for completeness.

In the following section ionic abundances are calculated relative to the He $^{+}$ . Line intensities normalized to He I  $\lambda 5876$ , which is undoubtedly emitted by the nebula, are used. The lines used to derive ionic abundances are listed in Table 7. Ionic abundances relative to He $^{+}$  will be escalated to H $^{+}$  by assuming a value for the He $^{+}/\text{H}^{+}$  abundance ratio and in further sections, total abundances will be derived.

<sup>4</sup>  $T_e(\text{He I})$  can be determined also using Porter et al. (2012, 2013) atomic data and PyNEB. We performed such a calculation, obtaining a temperature slightly higher that does not affect the abundance results. Therefore, we kept the value derived with Zhang et al. (2005) method.

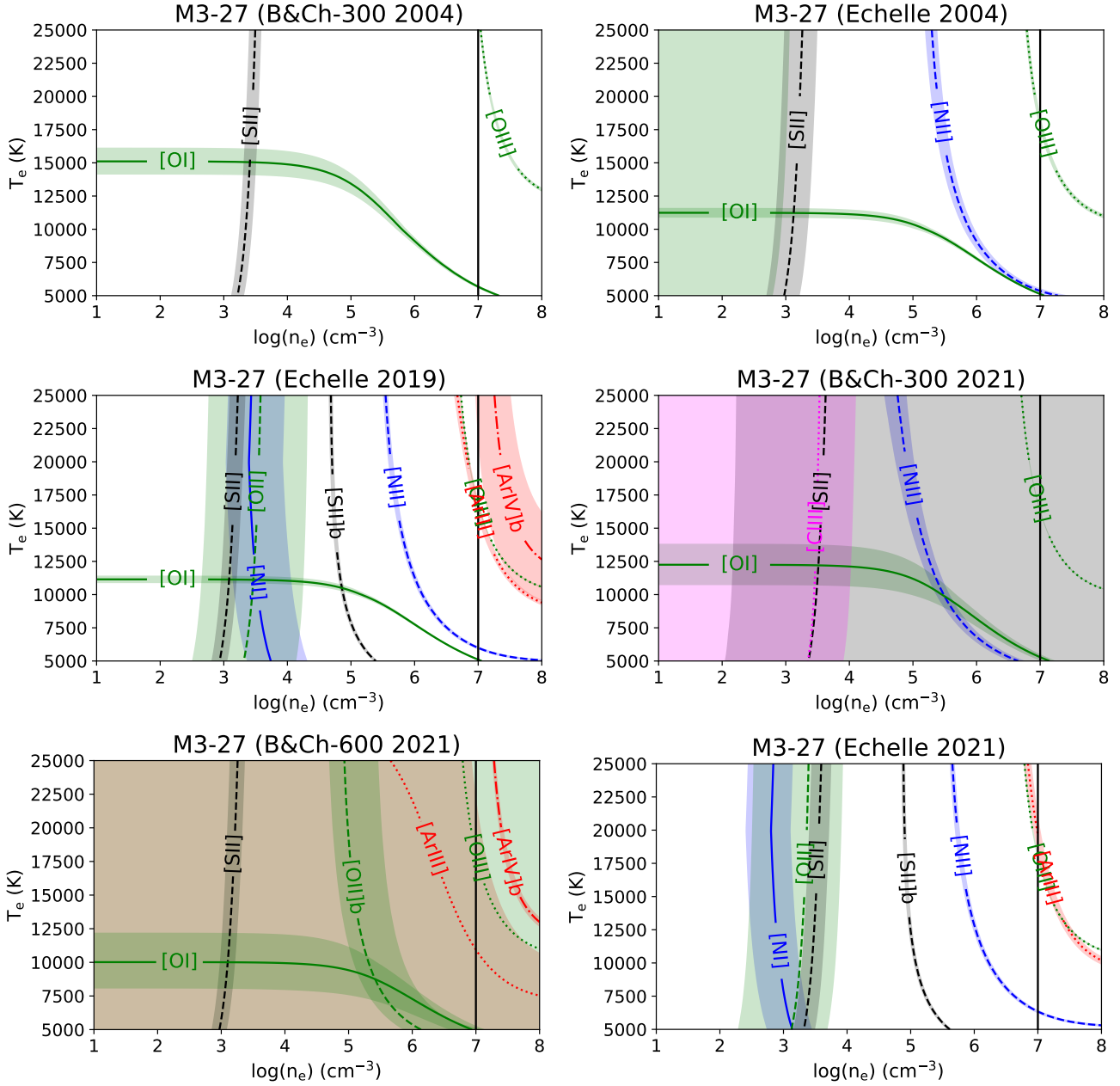


**Figure 6.** Diagnostic diagrams for density and temperature, derived with `PYNEB`. Sensitive CELs line ratios  $[O\text{ III}]\lambda\lambda(5007+4959)/4363$ ,  $[N\text{ II}]\lambda\lambda(6584+6548)/5755$ ,  $[Ar\text{ III}]\lambda\lambda 7136/5192$ ,  $[S\text{ II}]\lambda\lambda 6716/6731$ , and  $[O\text{ II}]\lambda\lambda 3726/3729$  are indicated. Coloured shadowed bands represent the 1 sigma rms error of each diagnostic.  $[O\text{ II}]b$ ,  $[S\text{ II}]b$  and  $[Ar\text{ IV}]b$  represent the line ratios  $\lambda\lambda 3727+7325+$ ,  $\lambda\lambda(6716+6731)/4068$  and  $\lambda\lambda 7170/4740$ , respectively. The vertical solid line in all diagrams represents a constant  $n_e$  of  $10^7\text{ cm}^{-3}$ .

### 5.1.1 Ionic abundances relative to $He^+$

To determine ionic abundances relative to  $He^+$  we used the data of REOSC-Echelle 2019 and B&Ch 2021 ( $300\text{ l mm}^{-1}$ ), which are the most complete spectra of those obtained at OAN-SPM. As said above, the line intensities were normalized to the intensity of  $He\text{ I } \lambda 5876$ . Ionic abundance of elements relative to  $He^+$  can be calculated using the next expression:

$$\frac{X^{+i}}{He^+} = \frac{I(\lambda)}{I(He\text{ I } \lambda 5876)} \frac{\epsilon_{He\text{ I } \lambda 5876}(He^+, \nu_{(He\text{ I } \lambda 5876)}, T_e)}{\epsilon_\lambda(X^{+i}, \nu_{ij}, T_e)} \quad (2)$$

Here  $\epsilon_\lambda$  is the emissivity of the line used to calculate the abun-

dance,  $\epsilon_{He\text{ I } \lambda 5876}$  is the emissivity of the  $He\text{ I } \lambda 5876$  line derived using the physical conditions previously determined for  $He\text{ I}$ , and  $I(\lambda)/I(He\text{ I } \lambda 5876)$  is the line intensity relative to  $He\text{ I } \lambda 5876$ . Line emissivities were calculated by using `PYNEB getEmissivity` task.

Following this method, ionic abundances from CELs relative to  $He^+$  were derived by assuming a unique value for  $T_e$  given by the  $[O\text{ III}]$  line diagnostic and two density zones as presented in Table 6. For the once ionized species and  $Fe^{+2}$  the  $n_e[S\text{ II}]$  was used except in the case of  $N^+$ , for which  $10^6\text{ cm}^{-3}$  was adopted as derived by the line ratio  $[N\text{ II}]\lambda\lambda(6584+6548)/5755$ . A density of  $10^7\text{ cm}^{-3}$  was used for the twice or more ionized species.

Ionic abundances from the recombination lines of the ions  $O^{+2}$ ,

**Table 6.** Electron temperatures and densities determined from CELs and ORLs for different epochs.  $T_e$  in K and  $n_e$  in  $\text{cm}^{-3}$ . Values marked with \* were determined by assuming a  $n_e = 1 \times 10^7 \text{ cm}^{-3}$ . Electron densities were derived by adopting the  $T_e$  determined from [O III]. :: indicates a very uncertain value.

Parameter/Obs.	Line ratio	B&Ch 2004 (300)	Echelle 2004	Echelle 2019	B&Ch 2021 (300)	B&Ch 2021 (600)	Echelle 2021
$T_e$ [O I]	(6364+6300)/5577	$15,000 \pm 1000$	$11,200 \pm 300$	$11,100 \pm 300$	$12,200^{+1500}_{-1300}$	$10,000^{+2560}_{-1340}$	$11,100 \pm 200$
$T_e$ [Ar III]*	7136/5192	—	—	$16,400 \pm 1000$	—	28,420::	$19,800^{+2100}_{-1700}$
$T_e$ [O III]*	(5007+4959)/4363	—	$18,100^{+1000}_{-900}$	$16,800^{+900}_{-600}$	$16,300 \pm 100$	$18,110^{+2550}_{-8550}$	$18,000 \pm 800$
Adopted	Unique zone	—	$18,100^{+1000}_{-900}$	$16,800^{+900}_{-600}$	$16,300 \pm 100$	$18,110^{+2550}_{-8550}$	$18,000 \pm 800$
$n_e$ [N I]	5200/5198	—	—	$2300^{+4100}_{-1100}$	—	—	$700^{+700}_{-400}$
$n_e$ [O II]	3729/3726	—	—	$2700^{+7200}_{-1900}$	—	—	$2200^{+3800}_{-1500}$
$n_e$ [S II]	6731/6716	$2600^{+600}_{-500}$	$1700^{+1400}_{-700}$	$1400 \pm 400$	$2200^{+5100}_{-1600}$	$1580^{+440}_{-510}$	$3400^{+1700}_{-1000}$
$n_e$ [Cl III]	5538/5518	—	—	—	$4600^{+12,700}_{-3800}$	—	—
$n_e$ [S II]b	(6716+6731)/4068	—	$24,100^{+4,500}_{-23,200}$	$63,300^{+5400}_{-62,100}$	—	—	$0.90^{+0.09}_{-0.88}$
$n_e$ [N II] ( $\times 10^5$ )	(6584+6548)/5755	—	$5.43^{+1.23}_{-0.97}$	$9.73^{+1.12}_{-0.95}$	—	—	$12.73^{+1.36}_{-1.17}$
$n_e$ [Ar IV]b ( $\times 10^7$ )	7170/4740	—	—	$5.76^{+2.94}_{-2.29}$	—	—	—
Adopted	Outer zone	$2600^{+600}_{-500}$	$1700^{+1400}_{-700}$	$1400 \pm 400$	$2200^{+4900}_{-1500}$	$1580^{+440}_{-510}$	$3400^{+1700}_{-1000}$
	Inner zone	$1 \times 10^7$	$1 \times 10^7$	$1 \times 10^7$	$1 \times 10^7$	$1 \times 10^7$	$1 \times 10^7$
$T_e$ H I (BJ)	—	—	—	11,500::	—	6280±3210	—
$T_e$ He I	7281/6678	$8500 \pm 400$	—	$8300 \pm 1000$	—	$10530 \pm 4550$	—
$n_e$ O II	4649/4661	—	—	$13,100^{+12,300}_{-10,200}$	—	—	—

**Table 7.** Lines used for ionic abundances calculation.

$X^{+i}$	Lines (Å)
N <sup>+</sup>	[N II] $\lambda\lambda 6548, 6584, 5755$
O <sup>+</sup>	[O II] $\lambda\lambda 3727+, 7325+$
O <sup>+2</sup>	[O III] $\lambda\lambda 4959, 5007, 4363$
Ne <sup>+2</sup>	[Ne III] $\lambda\lambda 3868, 3967$
S <sup>+</sup>	[S II] $\lambda\lambda 6716, 6731, 4068$
S <sup>+2</sup>	[S III] $\lambda 6312$
Cl <sup>+2</sup>	[Cl III] $\lambda\lambda 5517, 5537$
Ar <sup>+2</sup>	[Ar III] $\lambda\lambda 5192, 7136$
Ar <sup>+3</sup>	[Ar IV] $\lambda\lambda 4711, 4740, 7170$
Fe <sup>+</sup>	[Fe II] $\lambda 7155$
Fe <sup>+2</sup>	[Fe III] $\lambda\lambda 4659, 4701, 4755$

N<sup>+2</sup> and C<sup>+2</sup>, relative to He<sup>+</sup>, were computed in the same way and by assuming the  $T_e$  and  $n_e$  derived from recombination lines. The  $T_e$  used was the  $T_e(\text{He I})$ , while  $n_e(\text{O II})$  determined from the 2019 REOSC-Echelle data was assumed in all cases. C<sup>+2</sup> abundance was derived from C II  $\lambda 4267$ , O<sup>+2</sup> abundance was obtained from the lines of multiplet V1 and N<sup>+2</sup> abundance was derived from multiplet V3 lines.

The lines used to determine ionic abundances are those listed in Table 7. The derived ionic abundances are presented in Table 8.

From the ionic abundances relative to He<sup>+</sup> ( $X^{+i}/\text{He}^+$  in Table 8), ionic abundances relative to H<sup>+</sup> can be calculated by assuming that M 3-27 is a galactic disc PN with He/H = 0.11 (Kingsburgh & Barlow 1994) and that He/H = He<sup>+</sup>/H<sup>+</sup>, that is, we assume that there is neither He<sup>0</sup> nor He<sup>+2</sup> present in the nebula. In this way, the ionic abundances relative to H<sup>+</sup> were calculated as:

$$X^{+i}/H^+_{(\text{He}^+)} = X^{+i}/\text{He}^+ \times \text{He}^+/H^+ = 0.11 \times X^{+i}/\text{He}^+. \quad (3)$$

Their values are listed in Table 8. In this table we can appreciate that O<sup>+2</sup> is the most abundant ion of oxygen, being 2 or 3 orders of magnitude larger than O<sup>+</sup> calculated from  $\lambda 3727+$  lines (this is not the case of the O<sup>+</sup> abundance derived from the  $\lambda 7325+$  lines of the B&Ch 2021 data which is only one order of magnitude lower than

O<sup>+2</sup>). For the ions [N II], [O III], [Ar III] and [Ar IV] the abundances derived from the auroral and trans-auroral lines are similar indicating that used  $T_e$  and densities are correct.

The ionic abundances obtained this way can be compared to the values derived directly from H<sup>+</sup> (Appendix A). This comparison reveals that the ionic abundances from CELs,  $X^{+i}/H^+_{(\text{He}^+)}$ , are a factor of 1.2 lower than the values derived by using the H lines  $X^{+i}/H^+$ , possibly due to the assumption that He<sup>+</sup>/H<sup>+</sup> = He/H = 0.11. This assumption is one of those that produces large uncertainties in the abundances derived here. If we consider than He/H = 0.127, the ionic abundances derived from He<sup>+</sup> and from H<sup>+</sup> would be the same. This He/H value is at +1 standard deviation of the mean of the distribution calculated by Kingsburgh & Barlow (1994) for non-Type I galactic disc PNe, which is He/H = 0.112±0.015.

The ionic abundances  $X^{+i}/H^+_{(\text{He}^+)}$  derived from ORLs have diminished by a larger factor  $\sim 2$  when they are compared to the ionic abundances calculated directly by using H $\beta$  line,  $X^{+i}/H^+$ . This has consequences in the calculus of the ADF(O<sup>+2</sup>), presented in the same Table, which diminishes from 6.04 (Appendix A) to 3.26.

## 5.2 Total abundances

Total abundances of O/H, N/H, Ne/H, Ar/H, S/H, and Cl/H were computed from the  $X^{+i}/H^+_{(\text{He}^+)}$  ionic abundances (relative to He<sup>+</sup> and scaled to H<sup>+</sup>) and employing the Ionization Correction Factors, ICFs, by Kingsburgh & Barlow (1994). The ICF by Liu et al. (2000) was used for Cl/H abundance<sup>5</sup>. The derived abundance values are listed in Table 9, in units of  $12+\log(X/H)$ . Also the elemental abundances relative to O are listed. The N/H values marked with :: are extremely uncertain due to the large ICFs used.

<sup>5</sup> ICFs allow to correct total abundances for the presence of unseeing ions and the expressions used to obtain total abundance calculations are presented in Appendix B.

**Table 8.** Ionic abundances relative to He<sup>+</sup> derived from REOSC Echelle 2019 and B&Ch 2021 data. A unique value for  $T_e$  given by the [O III] line diagnosis and two density zones, as they are presented in Table 6, were adopted to determine ionic abundances. Abundances relative to H<sup>+</sup> (columns  $X^{+i}/H^{+}_{(He^{+})}$ ) were determined by assuming that He/H = 0.11, as derived by Kingsburgh & Barlow (1994) for non-type I disc PNe, and by assuming that the whole He in M 3-27 is single ionized (He/H = He<sup>+</sup>/H<sup>+</sup>).

Ion	$X^{+i}/He^{+}$		Ion	$X^{+i}/H^{+}_{(He^{+})}$	
	Echelle 2019	B&Ch 2021 (300)		Echelle 2019	B&Ch 2021 (300)
<b>ORLs</b>					
He <sup>+</sup> $\lambda$ 5876 Å	1	1	He <sup>+</sup> $\lambda$ 5876 Å	0.11	0.11
O <sup>2+</sup> $\lambda$ 4638 Å ( $\times 10^{-3}$ )	7.87 <sup>+2.52</sup> <sub>-2.94</sub>	—	O <sup>2+</sup> $\lambda$ 4638 Å ( $\times 10^{-4}$ )	8.63 <sup>+2.76</sup> <sub>-3.23</sub>	—
O <sup>2+</sup> $\lambda$ 4641 Å ( $\times 10^{-3}$ )	4.63 <sup>+0.54</sup> <sub>-0.57</sub>	—	O <sup>2+</sup> $\lambda$ 4641 Å ( $\times 10^{-4}$ )	5.08 <sup>+0.59</sup> <sub>-0.63</sub>	—
O <sup>2+</sup> $\lambda$ 4649 Å ( $\times 10^{-3}$ )	4.79 <sup>+1.00</sup> <sub>-0.49</sub>	—	O <sup>2+</sup> $\lambda$ 4649 Å ( $\times 10^{-4}$ )	5.25 <sup>+1.09</sup> <sub>-0.54</sub>	—
O <sup>2+</sup> $\lambda$ 4661 Å ( $\times 10^{-3}$ )	4.40 <sup>+1.24</sup> <sub>-1.93</sub>	—	O <sup>2+</sup> $\lambda$ 4661 Å ( $\times 10^{-4}$ )	4.83 <sup>+1.36</sup> <sub>-2.12</sub>	—
O <sup>2+</sup> $\lambda$ 4676 Å ( $\times 10^{-4}$ )	5.27 <sup>+1.44</sup> <sub>-1.45</sub>	—	O <sup>2+</sup> $\lambda$ 4676 Å ( $\times 10^{-3}$ )	5.78 <sup>+1.58</sup> <sub>-1.59</sub>	—
O <sup>2+</sup> V1 ( $\times 10^{-3}$ )	5.02 <sup>+0.46</sup> <sub>-0.50</sub>	—	O <sup>2+</sup> V1 ( $\times 10^{-3}$ )	5.50 <sup>+0.50</sup> <sub>-0.55</sub>	—
C <sup>2+</sup> $\lambda$ 4267 Å ( $\times 10^{-4}$ )	8.90 <sup>+3.37</sup> <sub>-3.03</sub>	—	C <sup>2+</sup> $\lambda$ 4267 Å ( $\times 10^{-5}$ )	9.76 <sup>+3.70</sup> <sub>-3.33</sub>	—
N <sup>2+</sup> $\lambda$ 5679 Å ( $\times 10^{-3}$ )	1.69 <sup>+0.65</sup> <sub>-0.51</sub>	—	N <sup>2+</sup> $\lambda$ 5679 Å ( $\times 10^{-4}$ )	1.86 <sup>+0.71</sup> <sub>-0.56</sub>	—
N <sup>2+</sup> V3 ( $\times 10^{-3}$ )	1.71 <sup>+0.63</sup> <sub>-0.55</sub>	—	N <sup>2+</sup> V3 ( $\times 10^{-4}$ )	1.87 <sup>+0.69</sup> <sub>-0.60</sub>	—
<b>CELs</b>					
O <sup>+</sup> Neb. ( $\times 10^{-7}$ )	5.74 <sup>+2.79</sup> <sub>-2.15</sub>	—	O <sup>+</sup> Neb. ( $\times 10^{-7}$ )	0.63 <sup>+0.31</sup> <sub>-0.24</sub>	—
O <sup>+</sup> Aur. ( $\times 10^{-4}$ )	—	1.46 <sup>+0.71</sup> <sub>-0.45</sub>	O <sup>+</sup> Aur. ( $\times 10^{-5}$ )	—	1.60 <sup>+0.78</sup> <sub>-0.49</sub>
O <sup>2+</sup> Neb. ( $\times 10^{-3}$ )	1.53 <sup>+0.28</sup> <sub>-0.29</sub>	1.70 <sup>+0.25</sup> <sub>-0.23</sub>	O <sup>2+</sup> Neb. ( $\times 10^{-4}$ )	1.68 <sup>+0.31</sup> <sub>-0.32</sub>	1.86 <sup>+0.28</sup> <sub>-0.25</sub>
O <sup>2+</sup> Aur. ( $\times 10^{-3}$ )	1.53 <sup>+0.27</sup> <sub>-0.29</sub>	1.68 <sup>+0.19</sup> <sub>-0.14</sub>	O <sup>2+</sup> Aur. ( $\times 10^{-4}$ )	1.68 <sup>+0.30</sup> <sub>-0.32</sub>	1.84 <sup>+0.21</sup> <sub>-0.15</sub>
N <sup>+</sup> Neb. ( $\times 10^{-5}$ )	2.09 $\pm$ 0.28	2.01 <sup>+0.26</sup> <sub>-0.23</sub>	N <sup>+</sup> Neb. ( $\times 10^{-6}$ )	2.29 $\pm$ 0.31	2.20 <sup>+0.28</sup> <sub>-0.26</sub>
N <sup>+</sup> Aur. ( $\times 10^{-5}$ )	1.15 <sup>+0.19</sup> <sub>-0.18</sub>	2.01 <sup>+0.26</sup> <sub>-0.24</sub>	N <sup>+</sup> Aur. ( $\times 10^{-6}$ )	1.26 <sup>+0.21</sup> <sub>-0.19</sub>	2.21 <sup>+0.28</sup> <sub>-0.26</sub>
Ne <sup>2+</sup> ( $\times 10^{-4}$ )	3.77 $\pm$ 0.61	5.44 <sup>+0.74</sup> <sub>-0.51</sub>	Ne <sup>2+</sup> ( $\times 10^{-5}$ )	4.13 $\pm$ 0.67	5.96 <sup>+0.81</sup> <sub>-0.56</sub>
Ar <sup>2+</sup> Neb. ( $\times 10^{-6}$ )	6.51 <sup>+1.08</sup> <sub>-0.94</sub>	7.01 <sup>+1.17</sup> <sub>-1.12</sub>	Ar <sup>2+</sup> Neb. ( $\times 10^{-7}$ )	7.13 <sup>+1.18</sup> <sub>-1.03</sub>	7.69 <sup>+1.28</sup> <sub>-1.23</sub>
Ar <sup>2+</sup> Aur. ( $\times 10^{-6}$ )	6.33 <sup>+0.91</sup> <sub>-0.99</sub>	—	Ar <sup>2+</sup> Aur. ( $\times 10^{-7}$ )	6.93 <sup>+1.00</sup> <sub>-1.09</sub>	—
Ar <sup>3+</sup> Neb. ( $\times 10^{-7}$ )	7.79 <sup>+3.29</sup> <sub>-3.04</sub>	—	Ar <sup>3+</sup> Neb. ( $\times 10^{-8}$ )	8.54 <sup>+3.60</sup> <sub>-3.33</sub>	—
Ar <sup>3+</sup> Aur. ( $\times 10^{-7}$ )	15.17 <sup>+2.99</sup> <sub>-2.77</sub>	—	Ar <sup>3+</sup> Aur. ( $\times 10^{-8}$ )	16.62 <sup>+3.28</sup> <sub>-3.02</sub>	—
S <sup>+</sup> Neb. ( $\times 10^{-7}$ )	1.34 <sup>+0.21</sup> <sub>-0.16</sub>	1.88 <sup>+1.56</sup> <sub>-0.49</sub>	S <sup>+</sup> Neb. ( $\times 10^{-8}$ )	1.48 <sup>+0.18</sup> <sub>-0.20</sub>	2.06 <sup>+1.71</sup> <sub>-0.53</sub>
S <sup>+</sup> T-aur. ( $\times 10^{-6}$ )	1.40 <sup>+0.22</sup> <sub>-0.15</sub>	—	S <sup>+</sup> T-aur. ( $\times 10^{-7}$ )	1.51 <sup>+0.23</sup> <sub>-0.16</sub>	—
S <sup>2+</sup> ( $\times 10^{-5}$ )	1.70 <sup>+0.31</sup> <sub>-0.24</sub>	1.63 <sup>+0.24</sup> <sub>-0.19</sub>	S <sup>2+</sup> ( $\times 10^{-6}$ )	1.87 <sup>+0.34</sup> <sub>-0.27</sub>	1.79 <sup>+0.27</sup> <sub>-0.21</sub>
Cl <sup>2+</sup> ( $\times 10^{-5}$ )	—	1.39 $\pm$ 0.69	Cl <sup>2+</sup> ( $\times 10^{-6}$ )	—	1.52 $\pm$ 0.76
Fe <sup>+</sup> ( $\times 10^{-6}$ )	1.45 <sup>+0.36</sup> <sub>-0.30</sub>	—	Fe <sup>+</sup> ( $\times 10^{-7}$ )	1.59 <sup>+0.39</sup> <sub>-0.33</sub>	—
Fe <sup>2+</sup> ( $\times 10^{-7}$ )	3.09 <sup>+0.58</sup> <sub>-0.47</sub>	—	Fe <sup>2+</sup> ( $\times 10^{-8}$ )	3.38 <sup>+0.64</sup> <sub>-0.52</sub>	—
ADF(O <sup>2+</sup> )	3.26 <sup>+0.81</sup> <sub>-0.61</sub>	—	ADF(O <sup>2+</sup> )	3.26 <sup>+0.81</sup> <sub>-0.61</sub>	—

## 6 EXPANSION VELOCITIES FROM LINES

Kinematic analysis from CELs and ORLs was performed for the data from REOSC-Echelle spectra, as these data offer the best spectral resolution ( $R \sim 18,000$ ) and cover a large range of wavelengths. For this analysis, the FWHMs of lines were measured and corrected by the effect of thermal and instrumental broadening. For the correction by thermal broadening the electron temperature adopted for each observation (as presented in Table 6) was used.

The FWHMs, expansion velocities  $v_{exp}$  (determined from FWHM of lines) and radial velocities  $v_{rad}$  of the observed lines in the three REOSC-Echelle spectra (2004, 2019 and 2021) are presented as online material together with the line fluxes and intensities for these observations. See an example of these data in Table 4. In Fig. 7 (left) we present the diagram of expansion velocities in function of ionization potentials for different CELs and ORLs (CELs represented by blue points, ORLs by red diamonds, green points correspond to CEL aurorals); it was constructed using REOSC-Echelle data from 2019 because this spectrum presents the largest number of measured lines. This diagram is equivalent to plot  $v_{exp}$  vs. distance to the central star, as it is expected that, due to the ionization structure of the nebula, ions more highly ionized are located nearer the central star (see e.g., the work by Peña et al. 2017, and references therein).

In Fig. 7 (left) it is observed that lines of [S II], [N II] and [S III] show velocities larger than 25 km s<sup>-1</sup>, while lines of [Fe III] and [O II] show smaller  $v_{exp}$  but have large error bars. Lines of [Ar III] and [O III] present  $v_{exp}$  of 25 and 21 km s<sup>-1</sup> and ions of larger ionization potentials like [Ne III] and [Ar IV] have the lowest  $v_{exp}$  of 20 and 18 km s<sup>-1</sup> respectively, thus CELs present a decreasing  $v_{exp}$ , from 26 to 18 km s<sup>-1</sup>, with increasing ionization potential. On the other hand, recombination lines show lower  $v_{exp}$  from about 15 to 19 km s<sup>-1</sup> which could be interpreted as if recombination lines are originated in a different zone than CELs, however the uncertainties are large, therefore the differences in velocities are not conclusive.

Also in Fig. 7, the green dots represent the  $v_{exp}$  of CELs auroral and transauroral lines of [S II], [N II], [O III], [Ar III] and [Ar IV], which show a different kinematic behaviour between both lines. It is observed that auroral (transauroral) lines of [S II], [N II] and [Ar III] show lower  $v_{exp}$  than their respective nebular lines, by about 7, 6 and 6 km s<sup>-1</sup>, respectively; however, for auroral and nebular lines of [O III] and [Ar IV] this difference is within the errors bars. This difference can be attributed to the suppression of nebular lines emission due to  $n_{crit}$  of these lines is lower than the  $n_e$ , which, as it was shown in previous sections, increases in inner parts of the nebula. In this way, in Fig. 7 (right) the differences in  $v_{exp}$  of nebular, auroral, and

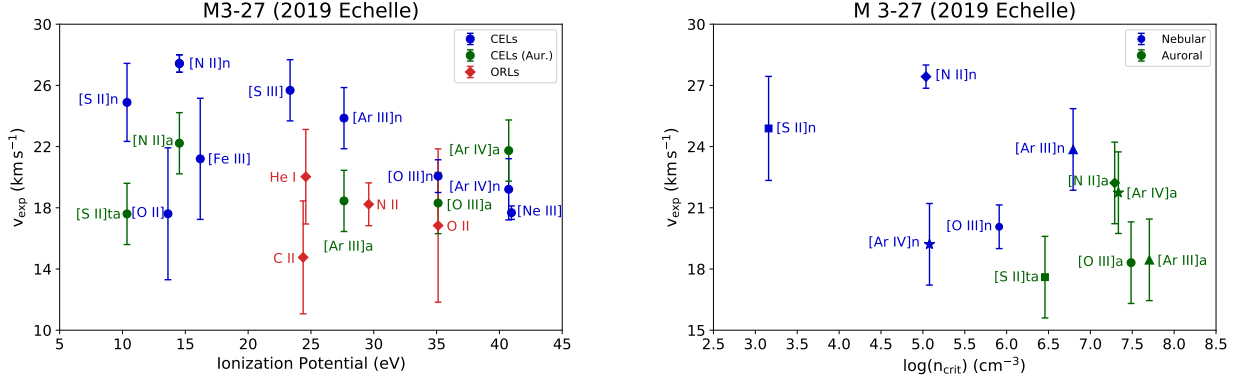


**Figure 7.** (Left) Expansion velocities of ions as a function of their ionization potentials for our REOSC-Echelle observations.  $v_{exp}$  of CELs are in blue (nebular lines) or green (auroral and trans-auroral lines),  $v_{exp}$  from ORLs are in red. Right figure: Expansion velocities of nebular (blue), auroral and trans-auroral lines (in green) vs. critical densities.

**Table 9.** Total abundances of M 3-27 from REOSC-Echelle spectrum determined using  $X^{+i}/H^+(He^+)$  ionic abundances. KB94 (Kingsburgh & Barlow 1994) and LS00 (Liu et al. 2000). :: indicates a very uncertain value.

$12 + \log(X/H)$	Echelle 2019	B&Ch 2021 (300)
He/H	11.04	11.04
O/H	$8.22^{+0.07}_{-0.09}$	$8.30 \pm 0.06$
N/H	9.79::	$7.44 \pm 0.17$
ICF(N) (KB94)	2568::	$12.32^{+5.91}_{-4.02}$
Ne/H	$7.62^{+0.07}_{-0.08}$	$7.81^{+0.05}_{-0.04}$
ICF(Ne) (KB94)	1	$1.09^{+0.05}_{-0.03}$
Ar/H	$5.90^{+0.06}_{-0.07}$	$6.16^{+0.07}_{-0.08}$
ICF(Ar) (KB94)	1	1.87
S/H	$7.26^{+0.11}_{-0.10}$	$6.47^{+0.09}_{-0.07}$
ICF(S) (KB94)	$9.50^{+1.10}_{-1.58}$	$1.65^{+0.21}_{-0.18}$
Cl/H	—	$6.40^{+0.20}_{-0.29}$
ICF(Cl) (LS00)	—	$1.67^{+0.22}_{-0.19}$
<i>log(X/O)</i>		
N/O (KB94)	1.55::	$-0.87 \pm 0.17$
Ne/O (KB94)	$-0.61 \pm 0.02$	$-0.49^{+0.03}_{-0.02}$
Ar/O (KB94)	$-2.32 \pm 0.03$	$-2.15 \pm 0.05$
S/O (KB94)	$-0.96^{+0.08}_{-0.06}$	$-1.83 \pm 0.07$
Cl/O (LS00)	—	$-1.89^{+0.17}_{-0.29}$

transauroral lines of the same ion are presented as a function of their critical densities. It is clear that lines with higher critical densities show lower  $v_{exp}$ .

## 7 DISCUSSION

The young PN M 3-27 presents several peculiarities that make difficult to perform a classical nebular analysis. The first problem is that the H I lines show P-Cygni type profiles with wide wings, these profiles are different in shape and in kinematic than the He I and heavy element profiles. This indicates that the H I lines are mainly emitted by the central star. We found that H $\alpha$  intensity has increased importantly between 1974 to 2004, suggesting important changes in the stellar emission in a period of 50 years.

In addition, several nebular line intensities have changed in the same period. To follow this evolution, the line intensities relative to H $\beta$  were analysed (see Fig. 2), but considering that H $\beta$  is mainly

emitted by the central star and might be changing, the line intensities relative to He I  $\lambda$ 5876 (which has a nebular profile) were also analysed (see Fig. 3). It is found that the line intensities of [O III] $\lambda$ 5007, [N II] $\lambda$ 6584 and [O II] $\lambda$ 3727+ have decreased significantly, while the auroral lines [O III] $\lambda$ 4363, [N II] $\lambda$ 5755, [O II] $\lambda$ 7325+ and also [Ne III] $\lambda$ 3869 present some small variations without important changes. This can be interpreted as a suppression of some nebular lines due to the large electron density in the inner nebular zone, with a value of about  $10^7$  cm<sup>-3</sup> which is in the limit or above the critical density of these lines. This value of  $n_e$ , estimated by the [O III]  $\lambda\lambda$ (5007 + 4959)/4363 line ratio is one order of magnitude larger than the value reported in the works by Adams (1975); Ahern (1978); Barker (1978) and Kohoutek (1968) of  $10^6$  cm<sup>-3</sup>, estimated using the same line ratio.

We do not attribute the changes of line intensities to recombination of the nebula because we do not find neither the diminution of the line intensities of high ionization species, like [Ne III] $\lambda$ 3869 or the auroral line [O III] $\lambda$ 4363, nor the increase of intensities of low ionization species lines, as [N II] $\lambda$ 5755 or [O II] $\lambda$ 7325+. Instead, the suppression of intensities is observed in lines having the lower critical densities.

Because of the details presented by H I lines, to determine the interstellar logarithmic reddening,  $c(H\beta)$ , we used a procedure based on the He I lines which provides a value between 0.39 and 0.63 in agreement with values derived by other authors from data of 1970 and calculated considering self-absorption,  $\sim 0.50$ – $0.75$ . It is interesting to note that Schlegel et al. (1998) and Schlafly & Finkbeiner (2011) have reported that the interstellar extinction in M 3-27 direction is  $c(H\beta)=0.31$ , therefore a part of the value derived for M 3-27 may be intrinsic in the nebula.

The estimates of electron density and temperature from CELs are complicated by the fact that density present a large contrast, with a value of about  $10^3$  cm<sup>-3</sup> in the outer zone, and about  $10^7$  cm<sup>-3</sup> in the inner zone. This high inner value causes that the line ratios usually employed to determine electron temperatures are now sensitive to density. With this density values of temperature between 16,000 and 18,000 K are found for our data. We adopted these values to derived ionic abundances of these observations from the CELs. It should be noted that Wesson et al. (2005) derived  $T_e = 13,000$  K assuming the same density for the inner zone. This occurred because the [O III] $\lambda$ 4363 intensity used by them (obtained in the year 2001) is lower than our value and the values reported for the seventies.

The electron temperature can also be determined from the recom-

bination lines of He I, obtaining values of 8300 – 10,500 K. Only for REOSC-Echelle 2019 data a temperature from the H I Balmer continuum with a value of 11,500 K was derived, nevertheless, this value is very uncertain and was not used for other calculations. It was found that the temperatures from ORLs are lower than the temperature from CELs, which is an expected result for planetary nebulae (this was first noticed by Peimbert 1971).

Another difficulty in M 3-27 analysis is the determination of total abundances from CELs. Even though the determination of total O/H abundance is simple (just by adding O<sup>+</sup> and O<sup>+2</sup> ionic abundances) due to O<sup>+</sup> abundance from [O II]λ3727+ lines is 3 or 4 orders of magnitude smaller than O<sup>+2</sup> abundance (see Table A1), ICFs for other elements that depend on O<sup>+</sup>, such as N and S, will be severely affected. For REOSC-Echelle spectra, this effect is evident for the ICF(N) by Kingsburgh & Barlow (1994), which would be extremely elevated (> 500) and therefore N/H total abundance would be very uncertain and overestimated. An alternative is to determine this ICF by using the auroral lines [O II] λ7325+, as it was done for the B&Ch spectra, in such a case the N/H abundance behaves accordingly to values of disc PNe. However, it is necessary to be cautious in the use of the N abundance derived using [O II] λ7325+ lines because, as it is well known, ionic abundances determined using this auroral line of O<sup>+</sup> are systematically larger than the derived from the nebular line (see e.g., Rodríguez 2020). Along with this problem is the diminution of O<sup>+</sup> nebular line intensity in a short period of time. For ICFs for Ar and Ne by Kingsburgh & Barlow (1994), their values are 1 for REOSC-Echelle observations, because they are based on O<sup>+2</sup>/O rates; in the case of Ar, in REOSC-Echelle spectra Ar<sup>+3</sup> is detected and so the correction is made considering the presence of this ion; for Boller & Chivens spectra this ion is not detected and, therefore, the correction was made using the ICF by Kingsburgh & Barlow (1994) that considers only the Ar<sup>+2</sup> abundance.

The C<sup>+2</sup>/H<sup>+</sup> abundance derived from the recombination line λ4267 is similar to the value reported by Wesson et al. (2005) from the same recombination line. These authors also derived C<sup>+2</sup>/H<sup>+</sup> from the ultraviolet line λ1909 intensity and adopting  $T_e = 13,000$  K, their derived value is similar to their value from λ4267 and would suggest an ADF(C<sup>+2</sup>) near 1. Previously Feibelman (1985) had estimated the C<sup>+2</sup>/H<sup>+</sup> value from the same line [C III]λ1909 but adopting  $T_e = 15,000$  K. Both C<sup>+2</sup>/H<sup>+</sup> values are very different due to the large dependence of CELs in temperature. Feibelman's value is more confident and would imply an ADF(C<sup>+2</sup>) of 1.86, more in agreement to the value derived for O<sup>+2</sup> and other elements.

Considering that H I lines seems to be emitted by the star, we have calculated the ionic abundances relative to the He<sup>+</sup> for the observations of REOSC-Echelle 2019 and B&Ch 2021, and transformed them to abundances relative to H<sup>+</sup> by assuming that He/H = He<sup>+</sup>/H<sup>+</sup> = 0.11. When possible, the ionic abundances derived from the auroral and nebular lines were computed to compare their values.

With this procedure the chemical abundances derived from CELs diminish by a factor of 1.2, while the chemical abundances derived from ORLs diminish by a factor of 2, when compared with the abundances derived relative to H<sup>+</sup> (see Appendix A). This effect could be due to the assumptions of  $T_e$  and  $n_e$  made to determine the emissivity of He<sup>+</sup> and the assumption made considering that He<sup>+</sup>/H<sup>+</sup> = He/H, that is, we consider that there is no He<sup>0</sup> in the nebula. To determine the contribution He<sup>0</sup> to He/H abundance is problematic and still is an open problem (see the discussion presented by Delgado-Inglada et al. 2014). This decrease in abundances has

effects on the determination of the ADF(O<sup>+2</sup>) which is 7.30 when abundances relative to H<sup>+</sup> are used (the average value from REOSC-Echelle spectra) and 3.26 if abundances relative He<sup>+</sup> are used (from REOSC-Echelle 2019 spectrum).

From the physical conditions and abundances derived from CELs and ORLs there are indications of the existence of two different plasmas in M 3-27 although the kinematics of CELs and ORLs are not so conclusive in this sense.

Our results so far are affected by the complexity of the abundance analysis in M 3-27. We consider that the best values of ionic abundances are those estimated relative to He<sup>+</sup> despite the several assumptions that were done for the He<sup>+</sup> abundance. Because of the problems for the ICFs that are based in O<sup>+</sup> abundance, we consider that the best values for total abundances are those derived with B&Ch 2021 data.

M 3-27 shares similar characteristics with the also young and compact PNe Vy 2-2 and IC 4997 that were analysed in our previous work (Ruiz-Escobedo & Peña 2022). These three PNe present a large density gradient showing an outer low-density zone with  $n_e \sim 10^3 - 10^4$  cm<sup>-3</sup> and an inner high-density zone with  $n_e \sim 10^5 - 10^7$  cm<sup>-3</sup>, being M 3-27 the nebula with the largest gradient. The three objects have sub-solar metallicities and show differences between the  $v_{exp}$  of nebular and auroral (or trans-auroral) lines of CELs of ions like [S II], [N II], [O III], [Ar III] and [Ar IV]. It is very possible that, as it was suggested by Zhang & Liu (2002), the standard temperature diagnostic ratios trend to overestimate  $T_e$  of the dense planetary nebulae resulting in an underestimation of total abundances.

Another important similarity between M 3-27 and IC 4997 is the variability of their line intensities and their physical conditions in short periods of time. Kostyakova & Arkhipova (2009) monitored the spectral evolution of IC 4997 for forty years. They claimed that  $n_e$  increased by a factor of 5, and  $T_e$  increased from 12,000 K to 14,000 K in a period of 20 yr while the nebular ionization degree has been growing with time. The central star seems to have increased its effective temperature from 37,000 – 40,000 K to 47,000 K in the same period, thus the nebular variations could be produced by changes in the central star which has been heating with time. IC 4997 also present a wide Hα line with a FWZI equivalent to 5,100 km s<sup>-1</sup> attributed to Raman scattering (Arrieta & Torres-Peimbert 2003). In addition Hyung et al. (1994), from 1990 – 1991 observations, found that Hα exhibits a P-Cygni profile. Nonetheless, Miranda et al. (2022) showed that during 2019 and 2020, the Hα profile exhibited only a single-peak profile and that its broad wings narrowed by a factor of 2.

Due to the above exposed, we consider that M 3-27 is an object very similar to IC 4997, in a previous evolutionary stage.

## 8 CONCLUSIONS

From high- and medium-spectral resolution obtained at OAN-SPM, México, from 2004 to 2021, we have analysed the characteristics of the young and dense PN M 3-27. During this epoch the central star shows profiles in emission type P-Cygni in the H I Balmer lines, in particular in Hα, Hβ, Hγ and Hδ, indicating the presence of a stellar wind. The stellar emission is variable as deduced mainly from the Hα emission. Due to the stellar emission of the Balmer lines, they cannot be used for determining c(Hβ) from the Balmer decrement, alternatively the He I lines were used and a value of about 0.47 was obtained (see Tab. 3).

M 3-27 is a very dense PN with an inner zone with density about 10<sup>7</sup> cm<sup>-3</sup>, which is larger than several critical densities of some

nebular lines. This makes difficult to determine electron temperatures with the usual nebular-auroral line intensity ratios. By adopting a density of  $10^7 \text{ cm}^{-3}$  as derived from our diagnostic diagrams, a  $T_e$  between 16,300 – 18,200 K was derived from CELs and employed for the calculus of ionic abundances. The inner density value seems to have increased in a period of 30 years from  $10^6 \text{ cm}^{-3}$  in the seventies (Adams 1975; Ahern 1978; Barker 1978; Kohoutek 1968) to  $10^7 \text{ cm}^{-3}$ , value found in this work.

Total abundances in M 3-27 were derived by calculating ionic abundances relative to  $\text{He}^+$  scaled to  $\text{H}^+$ , and by using the ICFs by Kingsburgh & Barlow (1994) and Liu et al. (2000). The values obtained for  $12+\log(\text{O}/\text{H})$  are sub-solar, between 8.23 and 8.30 (the solar value is  $12+\log(\text{O}/\text{H}) = 8.69$  as derived by Asplund et al. 2009). Our derived values for  $12+\log(\text{O}/\text{H})$  are smaller than the value presented by Wesson et al. (2005), probably due to the lower temperature used by these authors for abundance determinations. Total abundances of elements derived using ICFs based on  $\text{O}^+$  nebular line  $\lambda 3727+$  seem to be overestimated, due to the suppression of this line, so we adopted the total values determined using the auroral line  $\lambda 7325+$ . The abundance values of other elements relative to O indicate that M 3-27 is a disc nebula (Kingsburgh & Barlow 1994).

We have analysed the characteristics of M 3-27 in comparison with the also young and compact PNe VY 2-2 and IC 4997 which also present a large density gradient and variability of their line intensities. In particular M 3-27 is very similar to IC 4997 which has also showed stellar P-Cygni profile, nebular variations and wide  $\text{H}\alpha$  wings attributable to Raman scattering.

In the case of M 3-27, the important variations found on the  $\text{H}\alpha$  intensity suggest important changes on the central star emission. The variation of  $\text{H}\alpha$  profile, from the single-peaked profile reported by Tamura et al. (1990) to the P-Cygni profile, first reported by Miranda et al. (1997) and also found in our work, suggest that the stellar wind has strengthened. This changes in the stellar emission are reflected in the nebula, where it is found an increase in  $n_e$  from  $10^6 \text{ cm}^{-3}$  (in the seventies) to  $10^7 \text{ cm}^{-3}$  (after the year 2000) and the consequent suppression on the emission of lines with  $n_{crit}$  lower than the  $n_e$  of the nebula. Probably the stellar temperature has been changing with time too, however, this parameter was not explored in this work.

Forthcoming observations are needed to analyse the evolution of line intensities and nebular and stellar parameters of this very young planetary nebula, which has showed important changes in its characteristics in short periods of time.

## ACKNOWLEDGEMENTS

This work received partial support from Dirección General de Asuntos del Personal Académico-Programa de Apoyo a Proyectos de Investigación e Innovación Tecnológica (DGAPA-PAPIIT) IN111423, IN105020 and IN103519 and Consejo Nacional de Ciencia y Tecnología (CONACYT), México, project A1-S-15140. FR-E acknowledges scholarship by CONACYT, México. Helpful discussion and suggestions by Dr. Michael G. Richer are deeply acknowledged.

This work is based upon observations carried out at the Observatorio Astronómico Nacional at the Sierra San Pedro Mártir (OAN-SPM), Baja California, México. We thank the daytime and night support staff at the OAN-SPM for facilitating and helping to obtain our observations. The observations during 2021 were obtained by the resident astronomers at OAN-SPM as observers were not allowed at the observatory due to the COVID19 pandemic, so we are particularly grateful to them for their effort.

This work has made use of data from the European Space

Agency (ESA) mission *Gaia* (<https://www.cosmos.esa.int/gaia>), processed by the *Gaia* Data Processing and Analysis Consortium (DPAC, <https://www.cosmos.esa.int/web/gaia/dpac/consortium>). Funding for the DPAC has been provided by national institutions, in particular the institutions participating in the *Gaia* Multilateral Agreement.

## DATA AVAILABILITY

The data underlying this article will be shared on reasonable request to the corresponding author.

## REFERENCES

- Adams T. F., 1975, *ApJ*, **202**, 114  
 Ahern F. J., 1975, *ApJ*, **197**, 635  
 Ahern F. J., 1978, *ApJ*, **223**, 901  
 Arrieta A., Torres-Peimbert S., 2003, *ApJS*, **147**, 97  
 Asplund M., Grevesse N., Sauval A. J., Scott P., 2009, *ARA&A*, **47**, 481  
 Barker T., 1978, *ApJ*, **219**, 914  
 Bautista M. A., Fivet V., Ballance C., Quinet P., Ferland G., Mendoza C., Kallman T. R., 2015, *ApJ*, **808**, 174  
 Benjamin R. A., Skillman E. D., Smits D. P., 1999, *ApJ*, **514**, 307  
 Butler K., Zeippen C. J., 1989, *A&A*, **208**, 337  
 Capriotti E. R., 1964, *ApJ*, **140**, 632  
 Cardelli J. A., Clayton G. C., Mathis J. S., 1989, *ApJ*, **345**, 245  
 Delgado-Inglada G., Morisset C., Stasińska G., 2014, *MNRAS*, **440**, 536  
 Fang X., Storey P. J., Liu X. W., 2011, *A&A*, **530**, A18  
 Feibelman W. A., 1985, *PASP*, **97**, 404  
 Froese Fischer C., Tachiev G., 2004, *Atomic Data and Nuclear Data Tables*, **87**, 1  
 Gaia Collaboration et al., 2016, *A&A*, **595**, A1  
 Gaia Collaboration et al., 2023, *A&A*, **674**, A1  
 Galavis M. E., Mendoza C., Zeippen C. J., 1995, *A&AS*, **111**, 347  
 Galavis M. E., Mendoza C., Zeippen C. J., 1997, *A&AS*, **123**, 159  
 Hamuy M., Walker A. R., Suntzeff N. B., Gigoux P., Heathcote S. R., Phillips M. M., 1992, *PASP*, **104**, 533  
 Hyung S., Aller L. H., Feibelman W. A., 1994, *ApJS*, **93**, 465  
 Johansson S., Zethson T., Hartman H., Ekberg J. O., Ishibashi K., Davidson K., Gull T., 2000, *A&A*, **361**, 977  
 Kaufman V., Sugar J., 1986, *Journal of Physical and Chemical Reference Data*, **15**, 321  
 Kingsburgh R. L., Barlow M. J., 1994, *MNRAS*, **271**, 257  
 Kisielius R., Storey P. J., Ferland G. J., Keenan F. P., 2009, *MNRAS*, **397**, 903  
 Kohoutek L., 1968, *Bulletin of the Astronomical Institutes of Czechoslovakia*, **19**, 371  
 Kostyakova E. B., Arkipova V. P., 2009, *Astronomy Reports*, **53**, 1155  
 Lee H.-W., Hyung S., 2000, *ApJ*, **530**, L49  
 Liu X. W., Storey P. J., Barlow M. J., Danziger I. J., Cohen M., Bryce M., 2000, *MNRAS*, **312**, 585  
 Liu X. W., Luo S. G., Barlow M. J., Danziger I. J., Storey P. J., 2001, *MNRAS*, **327**, 141  
 Luridiana V., Morisset C., Shaw R. A., 2015, *A&A*, **573**, A42  
 McLaughlin B. M., Bell K. L., 2000, *Journal of Physics B Atomic Molecular Physics*, **33**, 597  
 Mendoza C., 1983, in Aller L. H., ed., *IAU Symposium Vol. 103, Planetary Nebulae*, pp 143–172  
 Mendoza C., Zeippen C. J., 1982, *MNRAS*, **198**, 127  
 Miranda L. F., Vazquez R., Torrelles J. M., Eiroa C., Lopez J. A., 1997, *MNRAS*, **288**, 777  
 Miranda L. F., Torrelles J. M., Lillo-Box J., 2022, *A&A*, **657**, L9  
 Peña M., Ruiz-Escobedo F., Rechy-García J. S., García-Rojas J., 2017, *MNRAS*, **472**, 1182

- Peimbert M., 1971, *Boletín de los Observatorios Tonantzintla y Tacubaya*, **6**, 29
- Pequignot D., Petitjean P., Boisson C., 1991, *A&A*, **251**, 680
- Podobedova L. I., Kelleher D. E., Wiese W. L., 2009, *Journal of Physical and Chemical Reference Data*, **38**, 171
- Porter R. L., Ferland G. J., Storey P. J., Detisch M. J., 2012, *MNRAS*, **425**, L28
- Porter R. L., Ferland G. J., Storey P. J., Detisch M. J., 2013, *MNRAS*, **433**, L89
- Quinet P., 1996, *A&AS*, **116**, 573
- Ramsbottom C. A., Bell K. L., 1997, *Atomic Data and Nuclear Data Tables*, **66**, 65
- Rodríguez M., 2020, *MNRAS*, **495**, 1016
- Ruiz-Escobedo F., Peña M., 2022, *MNRAS*, **510**, 5984
- Schlafly E. F., Finkbeiner D. P., 2011, *ApJ*, **737**, 103
- Schlegel D. J., Finkbeiner D. P., Davis M., 1998, *ApJ*, **500**, 525
- Schuster W. J., Parrao L., 2001, *Rev. Mex. Astron. Astrofis.*, **37**, 187
- Storey P. J., Hummer D. G., 1995, *MNRAS*, **272**, 41
- Storey P. J., Zeippen C. J., 2000, *MNRAS*, **312**, 813
- Storey P. J., Sochi T., Badnell N. R., 2014, *MNRAS*, **441**, 3028
- Storey P. J., Sochi T., Bastin R., 2017, *MNRAS*, **470**, 379
- Tamura S., Kazes I., Shibata K. M., 1990, *A&A*, **232**, 195
- Tayal S. S., 2011, *ApJS*, **195**, 12
- Tayal S. S., Gupta G. P., 1999, *ApJ*, **526**, 544
- Tayal S. S., Zatsarinny O., 2010, *ApJS*, **188**, 32
- Tresse L., Maddox S., Loveday J., Singleton C., 1999, *MNRAS*, **310**, 262
- Wesson R., Liu X.-W., Barlow M. J., 2005, *MNRAS*, **362**, 424
- Zamora S., Díaz Á. I., Terlevich E., Fernández V., 2022, *MNRAS*, **516**, 749
- Zhang H., 1996, *A&AS*, **119**, 523
- Zhang Y., Liu X. W., 2002, *MNRAS*, **337**, 499
- Zhang Y., Liu X. W., Liu Y., Rubin R. H., 2005, *MNRAS*, **358**, 457

## APPENDIX A: IONIC AND TOTAL ABUNDANCES RELATIVE TO H

From the line intensities relative to  $H\beta = 100$  which are listed in Table 4 ionic abundances relative to  $H^+$  were determined for all the epochs of observations. As was explained in Section 5.1, the routine *get.IonAbundance* from PYNEB was used. The procedure is the same as in Section 5.1, a unique value for  $T_e$  given by the [O III] line diagnostic and two density zones as presented in Table 6 were adopted to determine ionic abundances. For the once ionized species and  $Fe^{+2}$  the  $n_e[S II]$  was used except in the case of  $N^+$  for which  $10^6 \text{ cm}^{-3}$  was adopted. A density of  $10^7 \text{ cm}^{-3}$  was used for the twice or more ionized species. Again when possible, the ionic abundances derived from the auroral and nebular lines were computed to compare their values. The lines employed are those listed in Table 7. The derived values of ionic abundances are presented in Table A1.

As we concluded in Section 5.1, in Table A1 we can also appreciate that  $O^{+2}$  is the most abundant ion of oxygen, being 2 or 3 orders of magnitude larger than  $O^+$  calculated from  $\lambda 3727+$  lines and only one order of magnitude if  $O^+$  abundance is derived from the  $\lambda 7325+$  lines of the B&Ch 2021 data. And again for the ions [N II], [O III], [Ar III] and [Ar IV] the abundances derived from the auroral and trans-auroral lines are similar indicating that  $T_e$  and densities used are correct.

Considering all the above, we adopted the abundances of  $S^+$ ,  $N^+$ ,  $O^{+2}$ ,  $Ar^{+2}$  and  $Ar^{+3}$  derived from the nebular lines except in the case of  $N^+$  from B&Ch, for which the abundance derived from  $\lambda 5755$  was adopted<sup>6</sup>.

<sup>6</sup> The correction of the intensity of the auroral line [N II]  $\lambda 5755$  was presented in Section 5. The value of the recombination contribution was  $< 7\%$ .

In general, the ionic abundances relative to  $H^+$  derived from both REOSC-Echelle and B&Ch spectra are similar.

### A0.1 Abundances from ORLs

$He^+$  abundance was derived from the line  $He I \lambda 5876$ .  $n_e$  derived from  $O II \lambda \lambda 4649/4661$  determined from REOSC-Echelle 2019 spectrum was assumed for all observations.  $T_e(He I)$  as presented in Table 6 was used for these calculations. For the REOSC-Echelle 2004 observation the value determined from B&Ch ( $300 \text{ l mm}^{-1}$ ) observation from the same year was assumed, while for REOSC-Echelle and B&Ch ( $300 \text{ l mm}^{-1}$ ) 2021 observations, the  $T_e(He I)$  from REOSC-Echelle 2019 was assumed. All the values are presented in Table A1.

ORLs abundances of ions of heavy elements,  $O^{+2}$ ,  $N^{+2}$  and  $C^{+2}$ , were only determined from REOSC-Echelle spectra. As made explicit in §5.1 the  $T_e$  used for all cases was the  $T_e(He I)$  determined following Zhang et al. (2005) methodology, while  $n_e(O II)$  determined from the 2019 REOSC-Echelle data was assumed for all cases.  $C^{+2}$  abundance was derived from  $C II \lambda 4267$ ,  $O^{+2}$  abundance was obtained from the lines of multiplet VI and  $N^{+2}$  abundance was derived from multiplet V3 lines. All these ionic abundances are also listed in Table A1.

The average ADFs( $O^{+2}$ ) derived from these calculation is 7.37, similar to the ADF derived by Wesson et al. (2005) and larger than the ADF obtained by using  $He^+$  in the determination of ionic abundances.

### A1 Total abundances relative to H (based on ionic abundances relative to $H^+$ )

The abundances of He/H, O/H, N/H, Ne/H, Ar/H, S/H, and Cl/H were calculated from the ionic abundances presented in the subsections above and, the same as in §5, the ICFs by Kingsburgh & Barlow (1994) and by Liu et al. (2000) were used. The abundance results for observations from 2004 to 2021 are presented in Table A2 where the abundances relative to O are also listed, in logarithmic scale. To determine the He abundance only the  $He^+$  was considered because no emission from  $He^{+2}$  was detected in any of the spectra later than 2000.

The total abundances obtained for all the epochs are sub-solar ( $12 + \log(O/H)$  is between 8.18 and 8.37) and these values are lower than the values reported by Wesson et al. (2005) ( $12 + \log(O/H) = 8.60$ ) mainly due to the lower temperature used by these authors.

Due to the very low abundance of  $O^+$ , determined by using [O II]  $\lambda 3727+$  lines, the ICF for N/H, based on  $O/O^+$  is very large and uncertain, highly increasing the N/H value derived from REOSC-Echelle data. These N/H values are very uncertain and have been marked with :: in the tables. The N/H derived from the B&Ch data was obtained by using the ICF  $O/O^+$  derived from the auroral lines [O II]  $\lambda 7325+$ . This N/H value behaves accordingly with values for non Type I disc PNe. Wesson et al. (2005) derived a  $\log(N/O) = -0.77$  by using the line N III  $\lambda 1751$  and the ICF  $N/N^{+2} = O/O^{+2}$ , this value is very similar to the N/O values we found for the B&Ch data.

### APPENDIX B: IONIZATION CORRECTION FACTORS

ICFs used for the total abundances calculation are listed next.

- $\frac{He}{H} = \frac{He^+}{H^+}$ .
- $\frac{O}{H} = \frac{O^+ + O^{+2}}{H^+}$ .

**Table A1.** Ionic abundances relative to  $H^+$  for all epochs. A unique value for  $T_e$ , given by the [O III] line diagnostic and two density zones as they are presented in Table 6 were adopted to determine ionic abundances.

$X^{+i}/H^+$	Echelle 2004	Echelle 2019	B&Ch 2021 (300)	B&Ch 2021 (600)	Echelle 2021
<b>ORLs</b>					
He <sup>+</sup> (5876)	0.230 <sup>+0.020</sup> <sub>-0.022</sub>	0.241 <sup>+0.008</sup> <sub>-0.007</sub>	0.199 <sup>+0.039</sup> <sub>-0.031</sub>	0.176 ± 0.050	0.188 <sup>+0.005</sup> <sub>-0.004</sub>
O <sup>2+</sup> × 10 <sup>-4</sup> (4638)	—	1.37 <sup>+0.64</sup> <sub>-0.39</sub>	—	—	—
O <sup>2+</sup> × 10 <sup>-4</sup> (4641)	—	1.12 ± 0.13	—	—	1.10 <sup>+0.23</sup> <sub>-0.22</sub>
O <sup>2+</sup> × 10 <sup>-4</sup> (4649)	1.35 <sup>+0.59</sup> <sub>-0.42</sub>	1.14 <sup>+0.29</sup> <sub>-0.12</sub>	—	—	1.17 <sup>+0.27</sup> <sub>-0.17</sub>
O <sup>2+</sup> × 10 <sup>-4</sup> (4650)	—	—	—	—	1.12 <sup>+0.46</sup> <sub>-0.56</sub>
O <sup>2+</sup> × 10 <sup>-4</sup> (4661)	—	1.06 <sup>+0.29</sup> <sub>-0.41</sub>	—	—	0.92 <sup>+0.36</sup> <sub>-0.42</sub>
O <sup>2+</sup> × 10 <sup>-4</sup> (4676)	—	1.26 <sup>+0.36</sup> <sub>-0.33</sub>	—	—	1.89 <sup>+0.46</sup> <sub>-0.45</sub>
O <sup>2+</sup> × 10 <sup>-4</sup> (V1)	1.21 <sup>+0.12</sup> <sub>-0.09</sub>	1.22 <sup>+0.11</sup> <sub>-0.12</sub>	—	—	1.17 <sup>+0.14</sup> <sub>-0.15</sub>
C <sup>2+</sup> × 10 <sup>-4</sup> (4267)	—	2.17 <sup>+0.80</sup> <sub>-0.72</sub>	—	—	2.25 <sup>+0.68</sup> <sub>-0.65</sub>
N <sup>2+</sup> × 10 <sup>-4</sup> (5679)	6.41 <sup>+2.24</sup> <sub>-1.85</sub>	4.06 <sup>+1.59</sup> <sub>-1.21</sub>	—	—	2.14 <sup>+0.95</sup> <sub>-0.76</sub>
N <sup>2+</sup> × 10 <sup>-4</sup> (V3)	6.05 <sup>+1.72</sup> <sub>-1.88</sub>	3.84 <sup>+1.37</sup> <sub>-1.18</sub>	—	—	2.05 <sup>+0.81</sup> <sub>-0.72</sub>
<b>CELs</b>					
O <sup>+</sup> × 10 <sup>-7</sup> (Neb.)	2.57 <sup>+1.65</sup> <sub>-1.58</sub>	0.73 <sup>+0.37</sup> <sub>-0.29</sub>	—	6.56 ± 4.40	1.42 <sup>+0.63</sup> <sub>-0.51</sub>
O <sup>+</sup> × 10 <sup>-6</sup> (Aur.)	—	—	18.90 <sup>+8.44</sup> <sub>-6.33</sub>	15.59 ± 1.65	—
O <sup>2+</sup> × 10 <sup>-4</sup> (Neb.)	1.53 <sup>+0.36</sup> <sub>-0.30</sub>	1.99 ± 0.39	2.14 ± 0.21	1.55 ± 0.21	1.58 <sup>+0.34</sup> <sub>-0.31</sub>
O <sup>2+</sup> × 10 <sup>-4</sup> (Aur.)	1.52 <sup>+0.36</sup> <sub>-0.30</sub>	1.99 <sup>+0.37</sup> <sub>-0.39</sub>	2.16 ± 0.06	1.47 ± 0.37	1.59 <sup>+0.35</sup> <sub>-0.29</sub>
N <sup>+</sup> × 10 <sup>-6</sup> (Neb.)	2.45 <sup>+0.47</sup> <sub>-0.48</sub>	2.70 <sup>+0.36</sup> <sub>-0.37</sub>	2.54 ± 0.19	—	1.80 <sup>+0.25</sup> <sub>-0.22</sub>
N <sup>+</sup> × 10 <sup>-6</sup> (Aur.)	1.23 ± 0.22	1.39 <sup>+0.21</sup> <sub>-0.22</sub>	2.54 <sup>+0.19</sup> <sub>-0.18</sub>	3.65 ± 0.81	0.97 ± 0.16
Ne <sup>2+</sup> × 10 <sup>-5</sup>	2.86 <sup>+0.51</sup> <sub>-0.52</sub>	4.92 <sup>+0.82</sup> <sub>-0.77</sub>	5.70 ± 0.29	4.28 ± 0.11	4.15 <sup>+0.73</sup> <sub>-0.68</sub>
Ar <sup>2+</sup> × 10 <sup>-6</sup> (Neb.)	—	0.85 <sup>+0.11</sup> <sub>-0.13</sub>	0.90 ± 0.11	0.67 ± 0.15	0.57 <sup>+0.08</sup> <sub>-0.09</sub>
Ar <sup>2+</sup> × 10 <sup>-6</sup> (Aur.)	0.61 <sup>+0.14</sup> <sub>-0.13</sub>	0.82 ± 0.12	—	—	0.62 ± 0.10
Ar <sup>3+</sup> × 10 <sup>-7</sup> (Neb.)	—	10.04 <sup>+4.07</sup> <sub>-3.95</sub>	—	12.16 ± 0.12	9.05 <sup>+1.90</sup> <sub>-1.94</sub>
Ar <sup>3+</sup> × 10 <sup>-7</sup> (Aur.)	—	19.68 <sup>+3.84</sup> <sub>-3.29</sub>	—	—	—
S <sup>+</sup> × 10 <sup>-8</sup> (Neb.)	3.74 <sup>+0.83</sup> <sub>-0.60</sub>	1.73 <sup>+0.20</sup> <sub>-0.18</sub>	2.40 <sup>+1.77</sup> <sub>-0.63</sub>	2.45 ± 1.21	1.50 <sup>+0.32</sup> <sub>-0.22</sub>
S <sup>+</sup> × 10 <sup>-7</sup> (Taur.)	1.58 <sup>+0.27</sup> <sub>-0.22</sub>	1.81 ± 0.20	—	—	1.63 <sup>+0.16</sup> <sub>-0.18</sub>
S <sup>2+</sup> × 10 <sup>-6</sup>	1.56 ± 0.29	2.26 <sup>+0.36</sup> <sub>-0.35</sub>	2.16 <sup>+0.21</sup> <sub>-0.16</sub>	1.26 ± 0.50	1.32 <sup>+0.22</sup> <sub>-0.23</sub>
Cl <sup>2+</sup> × 10 <sup>-6</sup>	—	—	4.36 <sup>+2.40</sup> <sub>-1.88</sub>	—	—
Fe <sup>+</sup> × 10 <sup>-7</sup>	—	1.86 <sup>+0.43</sup> <sub>-0.36</sub>	—	—	—
Fe <sup>2+</sup> × 10 <sup>-8</sup>	—	4.02 <sup>+0.64</sup> <sub>-0.67</sub>	—	—	2.48 <sup>+0.53</sup> <sub>-0.49</sub>
ADF(O <sup>2+</sup> ) V1	8.40 <sup>+3.90</sup> <sub>-2.72</sub>	6.04 <sup>+1.69</sup> <sub>-1.08</sub>	—	—	7.47 <sup>+1.86</sup> <sub>-1.63</sub>

**Table A2.** Total abundances in 12+log(X/H) scale, determined for all the epochs. Relative abundances to O are presented in log(X/O) scale. KB94 (Kingsburgh & Barlow 1994) and LS00 (Liu et al. 2000). :: indicates a very uncertain value.

	Echelle 2004	Echelle 2019	B&Ch 2021 (300)	B&Ch 2021 (600)	Echelle 2021
<b>12+log(X/H)</b>					
He/H	11.36 ± 0.04	11.38 ± 0.01	11.30 <sup>+0.08</sup> <sub>-0.07</sub>	11.28 ± 0.44	11.27 ± 0.01
O/H	8.18 <sup>+0.10</sup> <sub>-0.09</sub>	8.30 <sup>+0.08</sup> <sub>-0.10</sub>	8.37 <sup>+0.04</sup> <sub>-0.05</sub>	8.28 ± 0.94	8.20 <sup>+0.08</sup> <sub>-0.09</sub>
N/H (KB94)	9.16::	9.86::	7.50 ± 0.17	7.58 ± 0.82	9.29::
ICF(N) (KB94)	575::	2603::	12.37 <sup>+5.84</sup> <sub>-4.04</sub>	1.13 ± 0.76	1100::
Ne/H	7.46 <sup>+0.07</sup> <sub>-0.09</sub>	7.69 ± 0.07	7.79 ± 0.02	7.37 ± 0.65	7.62 <sup>+0.07</sup> <sub>-0.08</sub>
ICF(Ne) (KB94)	1.00	1.00	1.09 <sup>+0.05</sup> <sub>-0.03</sub>	1.05 ± 0.05	1.00
Ar/H	6.06 <sup>+0.09</sup> <sub>-0.10</sub>	5.98 <sup>+0.06</sup> <sub>-0.07</sub>	6.23 <sup>+0.05</sup> <sub>-0.06</sub>	5.51 ± 0.42	5.82 <sup>+0.06</sup> <sub>-0.07</sub>
ICF(Ar) (KB94)	1.87	1.00	1.87	2.12 ± 0.68	1.00
S/H	6.97 <sup>+0.15</sup> <sub>-0.12</sub>	7.33 <sup>+0.11</sup> <sub>-0.10</sub>	6.55 ± 0.07	6.41 ± 0.64	6.97 <sup>+0.11</sup> <sub>-0.09</sub>
ICF(S) (KB94)	5.85 <sup>+1.60</sup> <sub>-0.98</sub>	9.54 <sup>+1.60</sup> <sub>-1.10</sub>	2.40 <sup>+0.21</sup> <sub>-0.16</sub>	1.04 ± 0.28	7.16 <sup>+1.19</sup> <sub>-0.93</sub>
Cl/H	—	—	6.86 <sup>+0.27</sup> <sub>-0.27</sub>	—	—
ICF(Cl) (LS00)	—	—	4.36 <sup>+2.40</sup> <sub>-1.88</sub>	—	—
<b>log(X/O)</b>					
N/O (KB94)	0.98::	1.56::	-0.86 ± 0.17	-0.70 ± 0.47	1.10::
Ne/O (KB94)	-0.73 ± 0.03	-0.61 ± 0.02	-0.58 <sup>+0.03</sup> <sub>-0.02</sub>	-0.91 ± 0.78	-0.58 ± 0.02
Ar/O (KB94)	-2.13 <sup>+0.07</sup> <sub>-0.08</sub>	-2.32 ± 0.03	-2.14 ± 0.05	-2.77 ± 0.87	-2.38 ± 0.03
S/O (KB94)	-1.21 <sup>+0.12</sup> <sub>-0.08</sub>	-0.96 <sup>+0.08</sup> <sub>-0.06</sub>	-1.83 <sup>+0.07</sup> <sub>-0.08</sub>	-1.87 ± 0.65	-1.22 ± 0.06
Cl/O (LS00)	—	—	-1.49 <sup>+0.19</sup> <sub>-0.29</sub>	—	—

**Table C1. Atomic parameters used in PYNEB calculations**

Ion	Transition probabilities	Collisional strenghts
N <sup>+</sup>	Froese Fischer & Tachiev (2004)	Tayal (2011)
O <sup>+</sup>	Froese Fischer & Tachiev (2004)	Kisielius et al. (2009)
O <sup>+2</sup>	Froese Fischer & Tachiev (2004) Storey & Zeippen (2000)	Storey et al. (2014)
Ne <sup>+2</sup>	Galavis et al. (1997)	McLaughlin & Bell (2000)
S <sup>+</sup>	Podobedova et al. (2009)	Tayal & Zatsarinny (2010)
S <sup>+2</sup>	Podobedova et al. (2009)	Tayal & Gupta (1999)
Cl <sup>+2</sup>	Mendoza (1983)	Butler & Zeippen (1989)
Ar <sup>+2</sup>	Mendoza (1983) Kaufman & Sugar (1986)	Galavis et al. (1995)
Ar <sup>+3</sup>	Mendoza & Zeippen (1982) Kaufman & Sugar (1986)	Ramsbottom & Bell (1997)
Fe <sup>+</sup>	Bautista et al. (2015)	Bautista et al. (2015)
Fe <sup>+2</sup>	Quinet (1996) Johansson et al. (2000)	Zhang (1996)
Ion	Effective recombination coefficients	
H <sup>+</sup>	Storey & Hummer (1995)	
He <sup>+</sup>	Porter et al. (2012, 2013)	
N <sup>+2</sup>	Fang et al. (2011)	
O <sup>+2</sup>	Storey et al. (2017)	
C <sup>+2</sup>	Pequignot et al. (1991)	

•  $\frac{N}{H} = \text{ICF}(N) \times \frac{N^+}{H^+}$ .  $\text{ICF}(N) = \frac{O}{O^+}$  (Kingsburgh & Barlow 1994).

•  $\frac{Ar}{H} = \text{ICF}(Ar) \times \frac{Ar^{+2}+Ar^{+3}+Ar^{+4}}{H^+}$ .  $\text{ICF}(Ar) = \frac{1}{1-N^+/N}$  if Ar<sup>+2</sup> and Ar<sup>+3</sup> are detected (Kingsburgh & Barlow 1994). If only Ar<sup>+2</sup> is detected:  $\frac{Ar}{H} = \text{ICF}(Ar) \times \frac{Ar^{+2}}{H^+}$   $\text{ICF}(Ar) = 1.87$  (Kingsburgh & Barlow 1994).

•  $\frac{Ne}{H} = \text{ICF}(Ne) \times \frac{Ne^{+2}}{H^+}$ .  $\text{ICF}(Ne) = \frac{O}{O^{+2}}$  (Kingsburgh & Barlow 1994).

•  $\frac{S}{H} = \text{ICF}(S) \times \frac{S^++S^{+2}}{H^+}$ .  $\text{ICF}(S) = \left[ 1 - \left( 1 - \frac{O^+}{O} \right)^3 \right]^{-1/3}$ . (Kingsburgh & Barlow 1994).

•  $\frac{Cl}{H} = \text{ICF}(Cl) \times \frac{Cl^{+2}}{H^+}$ .  $\text{ICF}(Cl) = \frac{S}{S^{+2}}$  (Liu et al. 2000).

## APPENDIX C: ATOMIC DATA

The atomic data used in PYNEB calculations are listed in Table C1.

This paper has been typeset from a  $\text{\TeX}/\text{\LaTeX}$  file prepared by the author.